frontiers in Energy Research

TYPE Methods
PUBLISHED 25 May 2026
DOI 10.3389/fenrg.2026.1801189

OPEN ACCESS

EDITED BY
Ellen B. Stechel,
Arizona State University, United States

REVIEWED BY
Wenhua Zuo,
Xiamen University, China
Ganesh Raghavendran,
Applied Materials, United States

*CORRESPONDENCE
Michael J. Dzara,
michael.dzara@nlr.gov

RECEIVED 01 February 2026
REVISED 19 March 2026
ACCEPTED 23 April 2026
PUBLISHED 25 May 2026

CITATION
Dzara MJ, Welborn SS, Crain C, Preefer MB, Slomski HS, Gorman BP, Nelson Weker J and Shulda S (2026) Image processing workflow yielding high contrast synchrotron nanoscale computed tomography data from Ni-YSZ electrodes.
Front. Energy Res. 14:1801189.
doi: 10.3389/fenrg.2026.1801189

Image processing workflow yielding high contrast synchrotron nanoscale computed tomography data from Ni-YSZ electrodes

Michael J. Dzara[1]*, Samuel S. Welborn[2], Christopher Crain[2], Molleigh B. Preefer[2], Heather S. Slomski[1,3], Brian P. Gorman[3], Johanna Nelson Weker[2] and Sarah Shulda[1]

[1]National Laboratory of the Rockies, Golden, CO, United States, [2]Stanford Synchrotron Radiation Lightsource, SLAC National Accelerator Laboratory, Menlo Park, CA, United States, [3]Colorado School of Mines, Golden, CO, United States

The operating lifetime of Ni-YSZ fuel electrodes used in solid oxide electrolysis cells and fuel cells (SOECs and SOFCs) is limited by Ni redistribution, one of the primary degradation mechanisms that must be overcome to extend the longevity and maximize the performance of SOECs and SOFCs. To achieve this, 3D microstructural data is needed to relate both initial performance and performance loss over time to microstructural properties and their evolution throughout operation under various conditions. However, 3D microstructure data remains relatively scarce within the literature due to multiple challenges in acquiring and analyzing such data reliably. This work presents a workflow for acquiring and processing synchrotron X-ray nanoscale computed tomography (nano-CT) data from Ni-YSZ electrodes. Parameters for each step in the nano-CT workflow are described up to the final result (a 3D reconstruction), with particular emphasis on image alignment using freely available software. Following the results of a parametric sweep of the image alignment step, high contrast, low signal-to-noise 3D nano-CT data is obtained with relatively short compute times. While the exact methods best suited to samples with different microstructural qualities, or similar Ni-YSZ nano-CT data obtained from other sources may deviate from the solution found herein, this work also generalizes the decision points and evaluation of each step to provide a starting point to adapt this workflow to other datasets.

KEYWORDS
image alignment, microstructure, nano-CT, Ni-YSZ, reconstruction algorithms, solid oxide cells, synchrotron X-ray, workflow development

1 Introduction

Solid oxide electrolysis cells (SOECs) and solid oxide fuel cells (SOFCs) are promising hydrogen production and electricity generation technologies. Comprised of layered ceramics and/or metals, SOECs electrochemically split steam into hydrogen and oxygen while SOFCs generate electricity from the electrochemical reaction of hydrogen and oxygen to produce steam and electrons within the range of 600 °C–800 °C (Hauch et al., 2020; Laguna-Bercero, 2012; Wolf et al., 2023). While the increased temperature results in a more efficient

reaction without the reliance on platinum group metal catalysts, it also drives numerous side reactions and multiple degradation pathways resulting in shorter device lifetimes, limiting the commercial viability of SOEC and SOFC technologies (Wang et al., 2020). The fuel electrode, which is responsible for the water splitting reaction in electrolysis mode and the reaction of oxygen ions with hydrogen to form steam in fuel cell mode, has been identified as a major contributor to performance losses due to materials degradation (Chen et al., 2013; Shri Prakash et al., 2014). Most often comprised of Ni metal and yttria stabilized zirconia (YSZ), fuel electrode degradation is primarily attributed to Ni instability, as the Ni particles have been observed to migrate towards or away from the YSZ electrolyte interface, redistribute and agglomerate, and detach/lose connectivity with the YSZ ion conducting phase (Mogensen et al., 2021; Mogensen et al., 2020; Mogensen et al., 2019; Mogensen et al., 2017). As the respective electrochemical reactions require three forms of transport (electronic, ionic, and gas phase mass transport) to occur, the activity and resistance of the fuel electrode is dependent on the amount of connected triple-phase boundary (TPB) sites and the properties of each conductive network (Jørgensen et al., 2015). Therefore, understanding and mitigating fuel electrode degradation is a 3D, 3-phase problem which requires microstructural characterization to link cell fabrication and processing parameters to initial performance, and operating conditions to extent of degradation (Kennouche et al., 2016a; Kennouche et al., 2016b; Lu et al., 2017).

Characterizing the 3D distribution of the three conducting phases present in Ni-YSZ requires a technique with adequate spatial and chemical resolution to isolate each phase from each other and to adequately evaluate surface/interface area to calculate TPB density (Lu et al., 2017; Bertei et al., 2017). While these requirements eliminate a number of common characterization techniques, use of multiple techniques to characterize 3D Ni-YSZ microstructure experimentally have been reported (Chiu et al., 2024; Cocco et al., 2013). Perhaps the most ubiquitous is focused ion beam coupled with scanning electron microscopy (FIB-SEM) as numerous studies featuring FIB-SEM of Ni-YSZ electrodes have been published; however this "slice and view" method is challenging, and the destructive nature of the technique can be limiting in any case when repeated measurements are desirable, such as *in situ* measurements with varied experimental conditions (Bertei et al., 2017; Hsu et al., 2018; Iwai et al., 2010; Joos et al., 2014; Joos et al., 2011; Mahbub et al., 2021; Trini et al., 2020; Trini et al., 2019). X-ray computed nanoscale tomography (nano-CT) is an alternative that has also been used to measure 3D microstructure of Ni-YSZ with growing frequency over the past several decades, particularly at synchrotron user facilities (Kennouche et al., 2016a; Kennouche et al., 2016b; Heenan et al., 2017; Nelson et al., 2012; Shearing et al., 2012). Unlike the more commonly seen micro-CT instrument, modern optics and monochromatic X-ray sources have enabled spatial resolution at the tens of nanometer scale, on par with FIB-SEM (Withers et al., 2021). Monochromatic X-ray sources result in an X-ray attenuation-based contrast of different materials–in the case of synchrotron X-rays where the energy can be tuned, this enables the researcher to maximize contrast by setting the incident energy just above or below the absorption edge of a relevant phase. Instruments with lab-based X-ray sources have also seen an increase in usage recently, however there are tradeoffs in accessibility, measurement time, X-ray source stability, and other factors (Heenan et al., 2017). At present, there are few such lab-based instruments while synchrotron facilities are open to user-access through a proposal system, so in this work we focused on synchrotron nano-CT. An emphasis is placed on presenting a generalized workflow from sample preparation through data processing and exploring parts of the data handling process in much more detail than what is typically published in device/material focused work to illuminate key factors in acquiring high quality 3D data for microstructural analysis of Ni-YSZ fuel electrodes.

Generally, nano-CT involves taking a number (theoretically described by the Crowther criterion (Crowther et al., 1970; Klug and Crowther, 1972), but in practice fewer images are sometimes adequate) of X-ray micrographs (XRMs) at different rotational angles in order to reconstruct a computed 3D object based on a stack of 2D projections reconstructed from information contained within the rotationally resolved XRMs (Klug and Crowther, 1972; Jacobsen, 2018). The process of analyzing Ni-YSZ microstructure with nano-CT can be split into the following steps: sample preparation, data acquisition, data pre-processing, XRM alignment, 3D reconstruction, optional post-processing, 3-phase semantic image segmentation, and microstructure property evaluation. Numerous approaches to each step in the workflow exist, and readers are directed to the literature for more extensive, generalized discussion on the technique (Withers et al., 2021; Tan et al., 2024). While each step is important towards accurate evaluation of Ni-YSZ microstructure, this work will primarily focus on image alignment, as this portion of the workflow is sometimes treated as a "black box" and experimental details are not often rigorously reported in applied work. Image alignment is necessary to correct for differences in exact sample location as the sample is rotated and successive XRMs are collected. One of the main sources of undesired sample motion is motor runout from the rotation stage, which results in sample jitter during rotation. While some modern instruments have incorporated sophisticated motion compensation to minimize this error, even in these cases the need for alignment is not completely eliminated (Stankevič et al., 2017; Wang et al., 2012). Historically, either a distinct feature of the sample or a fiducial marker which was placed on the sample's region of interest (ROI) in the form of a dense metal ball was used to aid in manual alignment of each XRM, however this approach is impractical for the large numbers of images usually needed to meet the Crowther criterion, impossible in certain sample morphology cases, and overly dependent on analyst input. Thus, several researchers have developed automated methods to iteratively align XRMs by jointly reconstructing (forward projecting the intersection of 2D images at different angles yielding a 3D object) and back projecting the reconstructed data as each 2D slice, allowing for cross correlation of the differences between the original 2D image and the back projected 2D slice following reconstruction. Differences allow for the shifts in sample features from angle to angle to be identified and deviation from the true center of rotation to be corrected, automatically aligning the stack of images as the process iterates (Gürsoy et al., 2017; Wang, 2020). While several options are freely available to implement such an approach, in this work, alignment and reconstruction are performed with TomoPyUI which was selected for its user-friendliness due to the ease with which data can be visualized throughout the processing pipeline (Welborn et al., 2024). TomoPyUI implements

the TomoPy (Gürsoy et al., 2014) framework for CT data handling, pre-processing, XRM alignment, and 3D reconstruction with the ASTRA toolbox (van Aarle et al., 2016; Pelt et al., 2016) integrated for efficient GPU-based computations enabling iterative reconstruction algorithms to be used in a time-efficient manner within a graphical user interface (GUI) that significantly reduces the barrier for entry to new analysts. Importantly, TomoPyUI enables visual inspection of the results of data processing steps in-line which is ideal for exploration of various steps and parameters within a step of a data processing workflow for efficient workflow development, which is the focus of this work.

This paper details the workflow of specimen preparation, data acquisition, XRM alignment, and 3D reconstruction of synchrotron nano-CT data collected on a Ni-YSZ fuel electrode using beamline 6-2c at the Stanford Synchrotron Radiation Lightsource (SSRL). Our approaches are laid out for specimen preparation and data acquisition in the Methods section, while the results of an evaluation of several different reconstruction algorithms and related variables and their impact on alignment success and reconstructed data quality are presented to identify best practices specific to Ni-YSZ samples and measurements performed at SSRL's 6-2c beamline. Discussion of methods to evaluate alignment and reconstruction protocols is also included to generalize the results found within this paper to other similar material systems, and nano-CT data collected at other facilities.

2 Methods

2.1 Sample characteristics

The SOEC used for this work was fabricated by previously reported methods, and the full description is available in the literature (Slomski et al., 2025; Zhu et al., 2025; Zhu et al., 2026). The electrode-supported cell features a 5–8 μm thick electrolyte comprised of 8 mol% yttria stabilized zirconia (8-YSZ), a 15–25 μm thick Ni-8YSZ fuel electrode functional layer (FL), and a 400–500 μm thick Ni-3YSZ support layer (SL). The initial ratio of NiO/YSZ used in the fuel electrode functional layer was 45/55 by wt. %. The green (as–fabricated) cell was then contacted and sealed to the testing apparatus before reduction of NiO to Ni *via* exposure to a H_2:N_2 blend at the cell operating temperature of 750 °C. Open circuit voltage was then monitored in a 97:3 H_2:H_2O blend until a stable value of 1.1 V was reached. At this stage, the cell was cooled and removed for analysis. More detailed information is available in the original publications, in which this sample was referred to as the "as reduced" baseline (Zhu et al., 2025; Zhu et al., 2026). While the focus of this work is only on data handling of one sample, the resulting optimized workflow was used to align and reconstruct all tomographic data in the associated work (Zhu et al., 2026), validating the efficacy of this method beyond a single solution.

2.2 Workflow overview

The process of measuring the Ni-YSZ fuel electrode with nano-CT is described in detail below while an overall depiction of the sample and resulting data is displayed in Figure 1. First, a ROI is isolated from the bulk SOEC and shaped to the desired dimensions. In this work, a columnar ROI with a diameter of ~8–12 μm and a height of > 50 μm is prepared to capture the cross-section of the YSZ electrolyte and the nearest portion of the Ni-YSZ fuel electrode in the axial dimension of the sample pillar (Figure 1a). XRMs are then collected at a number of angles that span a 180° rotation (Figure 1b). Within the raw XRM, intensity values are non-uniform as X-rays passing through different materials yield varying intensity due to their differences in X-ray absorption and density. Within this XRM, the Ni phase appears dark due to its high X-ray attenuation at the selected X-ray energy, whereas YSZ is lighter and pore space/background appears lightest. An inspection of the raw XRM intensity values from a single image prior to performing the entire tomography measurement is necessary to confirm that the detector is not saturated (instrument dependent), and to ensure adequate intensity values are counted to yield good signal-to-noise in the final reconstructed data. In this case, raw intensity values (averaged over 300 pixels in the Y-dimension) vary from 11k to 22k counts across the sample width following a 1 s exposure (Supplementary Figure S1). Following the full tomography dataset acquisition, the images are background corrected ($-\ln(I/I_0)$) and averaged, yielding a dark-field XRM (Figure 1c) at each angle in which Ni is the brightest phase. The XRMs are then aligned to account for any movement during rotation, and reconstructed into a 3D object, which can be handled as a stack of 2D slices or projections. A single 2D projection in the cross-sectional (axial) plane is displayed in Figure 1d following the optimized alignment and reconstruction procedure developed within this work. The 2D projection clearly shows grayscale contrast between the bright Ni, the intermediate gray YSZ, and the dark pore space.

2.3 Region of interest preparation

In the case of Ni-YSZ FLs, the ROI for nano-CT measurement is constrained to approximately the dimensions of the field-of-view (FoV) as the sample is dense and highly X-ray attenuating. Amongst lighter materials, interior nano-tomography (specimen ROI dimensions exceed detector dimensions) is feasible, however there will be a loss of contrast due to the longer X-ray path length through the specimen. For high resolution measurements, this delineates an ~10–20 μm ROI. Furthermore, nano-CT data quality is dependent on the transmittance of the sample which will vary with the dimension of the specimen, along with X-ray beam qualities (intensity and energy) and the porosity of the sample (Bailey et al., 2017). A columnar sample shape is preferred, so that the X-ray transmission pathlength is generally uniform as the sample is rotated, however this is not a strict requirement. To achieve this, a multi-step process (Supplementary Figure S2) was adapted from the literature (Bailey et al., 2017) using an Oxford Lasers A Series micromachining tool (Class 4 Laser, Class 1 Laser system, 532 nm wavelength, 10–500 ns pulse, max pulse energy of 1 mJ, max average power 10 W) for coarse milling and an FEI Helios 600i FIB for fine milling to produce an ~ 10 μm diameter sample ROI containing the YSZ electrolyte, Ni-YSZ FL, and a portion of the Ni-YSZ SL. A portion of the SOEC is mounted on an aluminum plate with the Ni fuel electrode contact facing up. An ~1 mm diameter disk is isolated from the SOEC by plan-view scribing of successively larger concentric circles from 1.0 mm to 1.2 mm diameters in 0.05 mm steps. This method is necessary to clear milling rubbish from the

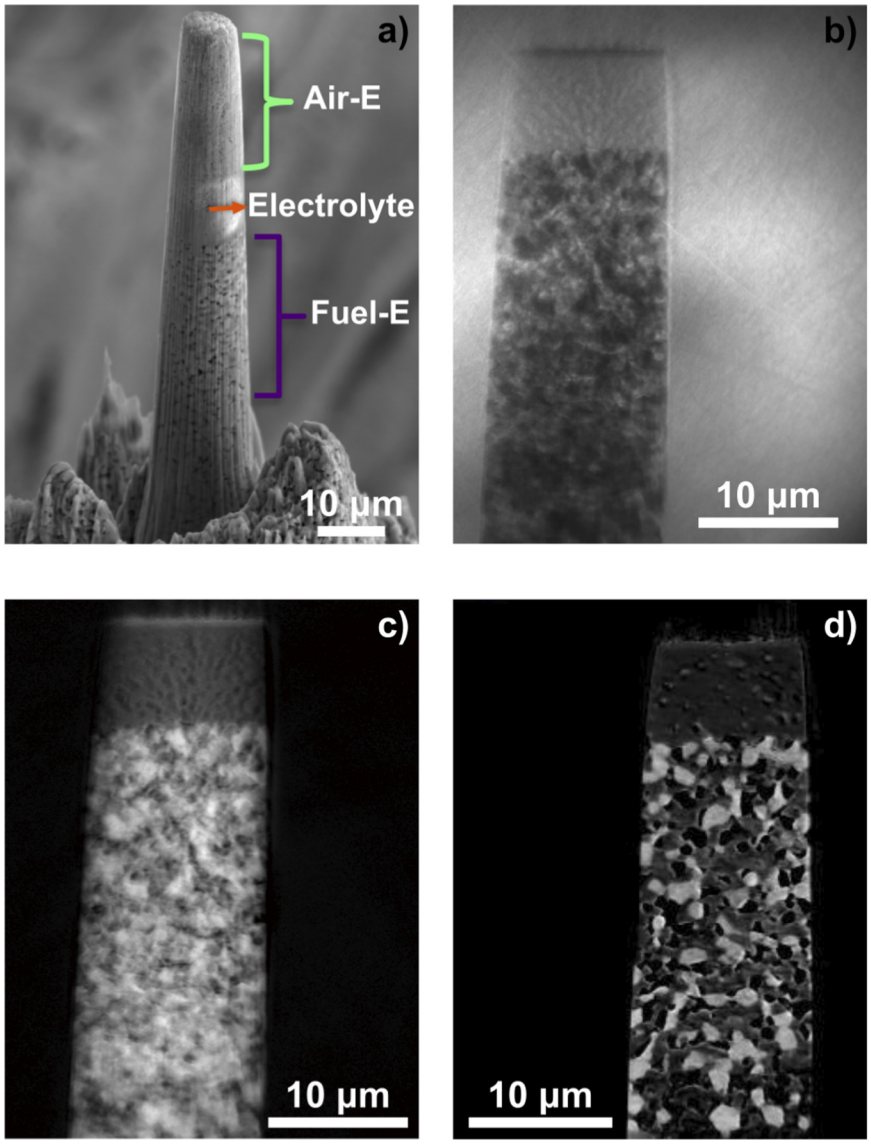

FIGURE 1
(a) An SEM image of a representative SOEC sample ROI after FIB thinning with the layers labelled (Air-E for air electrode and Fuel-E for fuel electrode), **(b)** an example of a single raw XRM, **(c)** an average of 10 dark-field background corrected XRMs at a given angle, and **(d)** a 2D projection sliced parallel to the axial dimension following image alignment and 3D reconstruction with the optimized workflow presented in this paper.

cut which accumulates over the course of milling. The laser power used was 0.3 W, a milling speed of 1 mm/s was used, and 100 passes are performed per step. Then, a 1 mm diameter, 5 mm long steel dowel is fixed to the fuel electrode back using a UV-cure resin. The 1 mm diameter sample ROI is thinned to ~0.2–0.1 mm diameter by laser-lathing an ~ 0.3 mm long pillar at 0.7 W. Finer thinning is performed down to 0.1–0.025 mm in successive lathing steps at a laser power of 0.2 W. The sample ROI is then transferred to a FIB for a final thinning with a 30 kV Ga ion beam in an FEI Helios 600i FIB, yielding a final diameter of ~8–16 µm at the YSZ/Ni-YSZ interface. The Ga ion thinning also serves to leave a clean specimen surface, as the laser lathe leaves a several micron thick external layer of damaged/redeposited material that is not representative of the true specimen (Bailey et al., 2017). Supplementary Figure S2 shows a similar sample ROI throughout the final thinning process, with the image of a final sample ROI presented in Figure 1a in which the layers of the SOEC are labelled.

2.4 Data acquisition

Beamline 6-2c at SSRL was used to acquire all nano-CT data. Samples were first aligned over 180° of rotation to ensure no portion of the ROI departs the FoV in the horizontal direction during the measurement. XRMs were collected above the Ni K_α absorption edge at an energy of 8,353 eV and with a × 10× objective magnification. An X-ray absorption near-edge spectroscopy (XANES) plot of the Ni K_α absorption edge is displayed in Supplementary Figure S3 to highlight the change in

Ni X-ray absorption above the edge, explaining the selection of incident energy to maximize Ni absorption. A 29.29 × 29.29 μm FoV with a resolution of 2,048 × 2,048 pixels was used resulting in a 14.3 nm pixel size. Due to the extremely high X-ray flux generated at synchrotron facilities, individual XRM exposure time was limited to 1s per exposure to avoid saturating the detector in the background regions of the image, and 10 exposures were collected at each angle, with a pixel binning factor of two yielding a final pixel/voxel size of 28.6 nm. Pixel binning two indicates that each set of four neighboring pixels in a square pattern are averaged to improve signal-to-noise at the cost of resolution. Reference images were collected with the sample moved entirely out of view, with 20 images collected and averaged every 180 images. Rotation over 180° was performed with data collected every 0.2°, for a total of 9010 XRMs (10 exposures per angle). An example of a resulting raw XRM is presented in Figure 1b.

2.5 Data pre-processing

Data handling was performed in either TXM Wizard or TomoPyUI (Welborn et al., 2024; Liu et al., 2012). Generally, the process involves averaging reference XRMs at each angle collected, correcting all raw XRMs with the averaged reference images, and then auto-aligning and averaging the background corrected XRMs at each angle, with an example of a resulting processed XRM displayed in Figure 1c. In TXM Wizard, this process is done step-wise and allows for visual inspection at each stage. In TomoPyUI, the pre-processing can be automatically performed during the data import. In both cases, further pre-processing such as 2D image filtering can be performed prior to alignment and reconstruction, however this optional step is omitted in this work.

2.6 XRM alignment

Due to fluctuations in exact sample position from angle to angle during rotation, image alignment is a crucial step in ensuring accurate interpretation of 3D data. The alignment process is performed in TomoPyUI, and the first step is setting the center of rotation. A guess for the center of rotation is made and a reconstruction is performed, and then a filtered 2D slice is backprojected. This process is performed over a range of center values, allowing the user to identify the center value that minimizes the crescent shaped "tuning fork" artifacts that occur when an inaccurate center value is used for reconstruction (Donath et al., 2006; Shepp et al., 1979). An example of 2D slices with correct, slightly off-center, and severely off-center selections as a function of previous alignment quality are displayed in Supplementary Figure S4 to highlight the presence of tuning fork artifacts used to identify the correct center of rotation. Additional results presented in Supplementary Figures S5, S6 display the impact of incorrect center of rotation guesses throughout the data handling process with associated discussion.

Within the center finding process, the user can define the reconstruction algorithm, number of reconstruction iterations, the step size and search range in center values around the original guess, the type of image filter to apply to the 2D slices, and the individual slice to display. In this work, the GridRec reconstruction algorithm is used to search a range of 100 center values in 1 pixel steps, and a parzen filter is applied to the 2D slice viewer. Slice selection was generally left at the default value of 512 (the vertical center of the FoV), displaying a portion of the Ni-YSZ FL several microns below the YSZ electrolyte interface. The resulting center of rotation used for alignment was 434 (value in pixels) unless otherwise specified, as in Supplementary Figures S5, S6.

The image alignment framework implemented in TomoPyUI is a joint iterative reconstruction and reprojection algorithm which has been described previously (Gürsoy et al., 2017). Briefly, a reconstruction is performed using a guess for the center of rotation as determined from the previously described step and with the reconstruction algorithm and settings selected by the user, then the reconstructed data is reprojected as a 2D image. The initial (or previous) projected data and that of the newly reconstructed and reprojected data are transformed into Fourier space where phase correlation is used to align the two datasets in the frequency domain to determine the X and Y shifts (Guizar-Sicairos et al., 2008). The calculated shifts from phase correlation in X and Y are applied and then the process repeats. This approach is advantageous for sparse datasets as it enables the use of iterative reconstruction approaches (Beister et al., 2012) that feature algebraic or statistical interpolation (discussed in more detail in Section 3.3) without nesting an iterative algorithm within an iterative framework which can cause divergence (Gürsoy et al., 2017). This method can take the entire dataset or a subset as the input for alignment by first setting an ROI within which phase correlation will be performed. Using a subset can decrease processing time and exclude homogeneous or erroneous portions of the tomography data that may delay the convergence of the alignment algorithm. In this work, the entire range of data is used in most cases, unless a phase correlation subset is specified as in 3.4. The reconstruction algorithm used is crucial to the efficacy of the alignment. TomoPyUI contains many traditional CPU-based algorithms and a few CUDA-capable algorithms from the ASTRA toolbox that are much more efficient due to their use of GPU resources (van Aarle et al., 2016; Pelt et al., 2016). In this work, 5 CUDA capable algorithms are evaluated: the classic analytical application of the inverse Radon transform - the filtered backprojection (FBP) implementing the Ram-Lak filter (Kak and Slaney, 2001; Ramachandran and Lakshminarayanan, 1971), simultaneous iterative reconstruction technique (SIRT) (Beister et al., 2012; Algebraic Reconstruction Algorithms, 2001; Gilbert, 1972; Gregor and Benson, 2008), simultaneous algebraic reconstruction technique (SART) (Beister et al., 2012; Algebraic Reconstruction Algorithms, 2001; Gilbert, 1972), conjugate gradient least squares (CGLS) (May et al., 2021; Scales, 1987; Cools et al., 2015), and maximum likelihood expectation maximization (MLEM) (Beister et al., 2012; Dempster and Laird, 1977; Lange and Carson). The differing attributes of each algorithm will be explored in more detail in Section 3.3.

For the given algorithm, the user then sets the center of rotation (automatically populated from the previous tab if used) selects the number of alignment iterations to be performed, the amount of padding (columns and rows with 0 intensity to add to the X and Y-axis) to enable application of alignment shifts, whether to downsample (perform additional pixel binning to smooth data and decrease compute times) the data during alignment, the amount of upsampling (pixel interpolation for phase correlation in Fourier space) to apply within the calculated XRM shifts,

whether to use a phase correlation subset of the full ROI, and any additional constraints specific to the reconstruction algorithm. Within this work, alignment iterations are varied by a 1–2–5 log-scale convention up to 500 iterations. Padding is set to 200 × 100 pixels (~2.86 × 1.43 μm) to accommodate applying the calculated shifts after alignment. Downsampling factors of 2, 4, and eight are applied in Section 3.4, although in the evaluation of other parameters no downsampling was used. The downsampling method is a pyramidal algorithm implemented from *dask* (Rocklin, , 2015). A phase correlation subset of 700 × 700 pixels set to include the edges of the sample on the X-axis, and the YSZ/Ni-YSZ interface in the Y-axis was used in Section 3.4. Upsampling (applied within Fourier space during cross-correlation of the joint reconstruction and reprojection images) was set to a factor of 50× for all alignments. No additional options were used in all cases; however, it should be noted that the ability to set constraints such as no negative values, modifying the image filter type in filtered reconstruction algorithms, and others are available should the user's data motivate further exploration of these parameters. In all cases, a new set of shifted XRMs, the value of each shift, and the convergence (relative mean square error or RMSE between the current and prior reconstruction) were saved for each alignment and are displayed.

2.7 Reconstruction

Following XRM alignment, a final 3D reconstruction is performed next. First, the center of rotation is reselected, as a much more accurate choice of rotation center can be performed on aligned data, which is clearly demonstrated in Supplementary Figure S4. A convention of finding the center of rotation at three, equally spaced slices offset by 256 pixels was used from a range of y-values from 256 to 768. This was selected to account for the possibility of off-axis rotation; however, generally all well-aligned datasets displayed an approximately constant center of rotation with respect to the rotational axis and multiple centers were likely unnecessary. In all cases, the reconstruction ROI was set to include all YSZ and Ni-YSZ data, while including minimal background on the edges of the sample. A single iteration of the FBP algorithm using the Ram-Lak filter was used in all cases. No change in data sampling was applied at the reconstruction step. All reconstructions were saved as a single tiff stack.

2.8 Reconstructed data handling

All 3D datasets were handled and analyzed using Dragonfly 2022.2 (Comet Inc.). The reconstructed data was imported with the cubic voxel size of 28.6 × 28.6 × 28.6 nm^3 manually input, as determined by the selection of X-ray incident energy and objective lens setting. Each dataset was then cropped to a rectangular prism containing ~6 × 6 × 16 μm^3 of data, with the axial dimension equal to roughly 16 μm and convention set so that the upper edge cuts through the YSZ/Ni-YSZ interface. Then, the cropped volume was converted to 8-bit to normalize the scale of grayscale values presented within all histograms, ranging from 0 to 255 in one integer bins. Grayscale images were contrast balanced to the same extent in all examples, with each 2D projection exported along with the outline of the cropped ROI used to produce the data's grayscale histogram. Signal to noise ratio (SNR) and contrast to noise ratio (CNR) were calculated using the below formulas, where in Equations 1, 2 μ is the mean grayscale value from an intra-phase ROI and σ is the standard deviation of the grayscale value from a ROI set in the background.

$$SNR = \frac{\mu}{\sigma} \tag{1}$$

$$CNR = \frac{\mu 1 - \mu 2}{\sigma} \tag{2}$$

To account for possible image gradients, five slices spaced ~2 μm apart along the vertical axis of the sample were used to select ROIs for SNR and CNR. On each slice, 3 ROIs are selected within the visibly distinct regions corresponding to each phase and the background, as shown in Supplementary Figure S7. In all cases, data is scaled to 8-bit for SNR and CNR calculations.

2.9 Workstation specifications

To qualify the compute times discussed within this work, a description of the workstation used for all data processing is included. A Dell Precision 5820 Tower running Windows 10 was used for all data processing. This workstation is equipped with an Intel Xeon W-23235 6 core, 3.8 GHz CPU, 128 GB RAM, and a NVIDIA RTX A4500 20 GB vRAM GPU with 7,168 CUDA cores. It should be noted that while TomoPyUI can be operated in the absence of a CUDA capable GPU, the ASTRA toolbox requires the use of a CUDA-enabled GPU and all reconstruction algorithms used for both alignment and 3D reconstruction of aligned data utilize the algorithms within the ASTRA toolbox for faster GPU-based computations (van Aarle et al., 2016; Pelt et al., 2016).

3 Results and discussion

This section focuses on displaying the impact of various parameters selected during the image alignment process. An optimal combination of parameters is determined for this dataset, however the solution presented herein may not be suitable for all similar measurements. Towards the goal of generalizing the image alignment portion of the nano-CT workflow to analysts working with various samples and data sources, we first discuss the tools with which we can evaluate the efficacy of a given image alignment approach.

3.1 Alignment and final data quality evaluation metrics

The alignment quality of a nano-CT dataset is most simply evaluated by inspecting the XRMs as a function of rotation angle visualized in a flipbook like video both before (Supplementary Video S1) and after alignment (Supplementary Video S2). Prior to alignment, the XRMs clearly show significant displacement on the X-axis and more moderate displacement on the Y-axis from angle to angle throughout the 180° rotation. Following alignment, minimal displacement is present when focused on fiducial markers such as the vertical edges of the sample, or the horizontal interface between Ni-YSZ FL and YSZ electrolyte layers. Note that the regions nearest to the

vertical edges of the ROI appear to flicker, which is due to the Y-axis displacement during rotation–as the sample extends through the vertical boundaries of the image ROI, different amounts of the sample are present in each XRM and the extrema only appear in a subset. These regions (~50 pixels or ~1.6 μm) are cropped and discarded to avoid an intensity gradient in analyzed data. Visual inspection of the aligned images during rotation is a direct way to observe the alignment quality, however subtle differences may be easier to detect and interpret with other tools.

In addition to rotation videos, several metrics to qualify alignment quality are presented within Figure 2, including sinograms (θ vs. X at a given Y value), a log-scale plot of RMSE between reconstruction and reprojection (called convergence) as a function of iteration, applied X and Y shifts, a grayscale 2D slice from the reconstructed 3D data, and the resulting histogram of grayscale intensity values from the final cropped 3D volume. A sinogram is presented for a given Y-value taken roughly from the middle of the sample ROI prior to any alignment (Figure 2a). This graph of intensity as a function of XRM angle at a given value on one of the Cartesian axes plotted against the other Cartesian axis known as a sinogram is equivalent to the plot of Radon-transforms (line integral of density of a function reducing a 2D plane to a 1D intensity profile for a given value) for a given slice, from which tomographic reconstruction can be performed (Withers et al., 2021; Crowther et al., 1970). Generally, the sinogram of a poorly aligned dataset will appear spiky and regions of high or low signal from the sample appear discontinuous, as in Figure 2a. While an alignment algorithm is running, the convergence between reconstruction and reprojection is updated each iteration (Figure 2b) alongside the X and Y shifts applied to the data (Figure 2c). These can be monitored while the alignment proceeds in real-time if desired. While RMSE plateauing can be an indication that high contrast, low noise data suitable for segmentation will be present in the final reconstructed volume, this is not guaranteed as RMSE can be low in well-aligned but noisy, low contrast data. This limitation will need to be overcome as data processing moves towards automation, and may be addressed through machine learning (ML) reconstruction algorithm implementation. Following alignment, the sinogram (Figure 2d) appears much smoother, and distinct features like the edge of the sample or regions of particularly high (Ni) or low (pores) signal are discernible across a span of values of θ and have minimal discontinuity, confirming a good quality alignment. Generally, the sinogram can be evaluated to confidently identify whether an alignment has failed, but subtle differences can be difficult to identify, and a good quality alignment does not guarantee high contrast, low noise data in the final reconstructed object. However, it is still advantageous to have the inline feedback within the alignment GUI provided by convergence and sinogram plots to quickly evaluate alignment parameters without performing a reconstruction or having to handle the 3D data in separate software.

After an alignment workflow appears to have converged, the final 3D reconstructed object is evaluated by visual inspection of the 2D grayscale projections (Figure 2e), and the resulting grayscale histogram (Figure 2f) of an internal ROI to determine the suitability of a dataset for subsequent 3-phase segmentation and quantitative analysis. Some degree of prior knowledge of the sample features such as phase fraction, feature size and distribution, and the presence of fiducials like the distinct YSZ/Ni-YSZ interface present in this sample is necessary to evaluate the data, and corroboration with other characterization techniques should be used when possible. As Ni-YSZ is a 3-phase system (pores, YSZ, and Ni are present in order of increasing brightness/grayscale value) the best possible histogram would feature three clearly separated peaks. An idealized dataset would contain clear local minima between each peak present at low percentages (many low count grayscale values between each peak), allowing most voxels to be clearly labelled as pore, YSZ, or Ni with complete confidence. However, even the data presented in Figure 2f following the optimized process presented herein contains regions between each peak in which it is uncertain whether the voxels at that grayscale value would belong to one phase or the other, largely due to image noise and resolution limitations in capturing the edge/interface of a phase where two phases are present in a single voxel. In Sections 3.3–3.5, SNR and CNR are calculated for each phase and phase combination, respectively. These metrics aid in evaluating data quality differences when histograms are very similar. Post-processing data through filtering and contrast enhancing operators can be performed to reduce the impact of noise, and certain segmentation techniques may be less impacted by data quality (Tan et al., 2024). Selection of post-reconstruction analysis tools will definitively impact the accuracy and reliability of the desired microstructural properties, however as the focus of this work is on the impact of the image alignment step, the qualities of the grayscale histogram are the ultimate metric used to evaluate XRM alignment and nano-CT data quality throughout this work.

3.2 Alignment dependence on reconstruction algorithm and number of iterations

Within the alignment framework implemented in TomoPyUI (Welborn et al., 2024), a joint-iterative reconstruction and reprojection approach (Gürsoy et al., 2017), there are several crucial inputs an analyst must decide upon and evaluate. We begin by exploring the five CUDA-capable GPU based reconstruction algorithms (FBP, SIRT, SART, CGLS, and MLEM) employed within the ASTRA toolbox as a reconstruction is performed in each iteration of this alignment approach. Other inputs are kept constant and explored in subsequent sections; a center of rotation value of 434 (pixels on the X-axis) was selected, the entire ROI is used for alignment, and no downsampling of data during alignment is applied. Alignments using each different reconstruction algorithm were performed with 10, 20, 50, 100, 200, and 500 iterations and then reconstructed (details in Section 2.7) to accommodate analysis of the 2D grayscale projection and grayscale histogram from an internal ROI selected from within the 3D object. Plots of convergence vs. iteration and applied X and Y shifts following alignment are displayed in Figure 3 for 50 and 500 iterations. Convergence occurs rapidly over the first 10 iterations with the MLEM reconstruction algorithm yielding the lowest RMSE value. Between 10 and 50 iterations, all algorithms change less from iteration to iteration, suggesting minimal change in applied shifts are occurring. Interestingly, each algorithm displays a peak after five iterations and before 50 iterations are reached, indicating that the algorithm has exited a local minimum and then continues to improve the alignment reaching lower RMSE values.

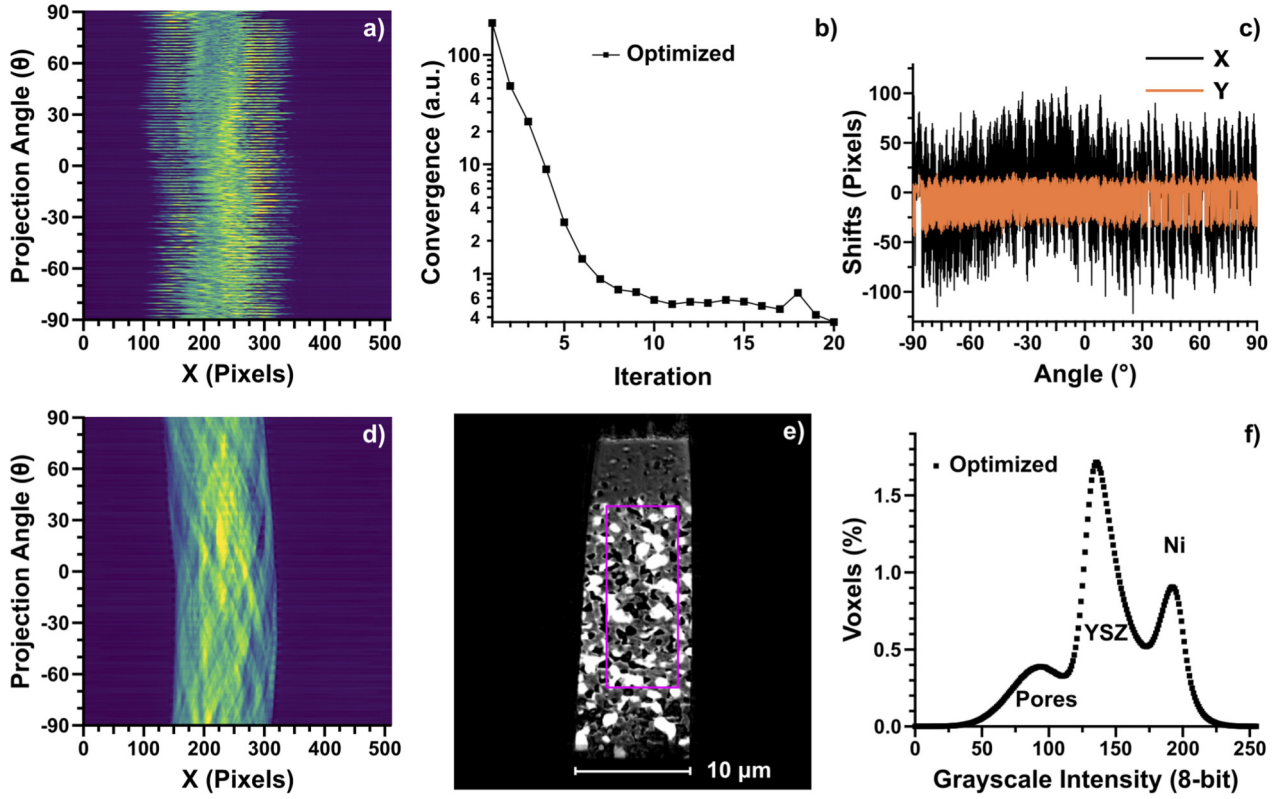

FIGURE 2
Data quality evaluation tools include **(a)** sinogram of the processed data pre-alignment at Y-value of 500 pixels which corresponds to mid-sample is displayed using a viridis lookup table to scale intensity values, **(b)** convergence (RMSE) plotted as a function of alignment iteration, **(c)** applied X and Y shifts following alignment, **(d)** sinogram of the aligned data at the same Y-value, **(e)** 2D grayscale projection of the reconstructed 3D volume sliced parallel to the axial dimension of the ROI with contrast balancing applied and a pink outline of the ROI cropped for histogram evaluation included, **(f)** an 8-bit histogram of the grayscale values normalized to the total number of voxels in the cropped ROI. All data corresponds to the final optimized data handling workflow.

As the alignment progresses from 50 to 500 iterations (Figure 3b), all reconstruction algorithms appear to plateau and no longer change significantly in RMSE. The lowest value is reached by FBP, despite also showing the slowest initial convergence. It is also noteworthy that the MLEM algorithm slowly increases in RMSE from its minimum value reached after ~25 iterations until convergence is reached after 100–150 iterations. Convergence plots for each additional alignment performed (10, 20, 100, and 200 iterations) using all reconstruction algorithms are displayed in Supplementary Figures S8a,b, S9a,b. Examining the applied X and Y shifts, some slight differences are present but largely the same values are obtained from each reconstruction algorithm, especially after 500 iterations (Figure 3d). The largest difference between 50 and 500 iterations occurs for FBP as this algorithm appeared to result in a continuous decreasing positive offset in Y-shifts from −90 to ~30° after 50 iterations which is no longer present after 500 iterations. It is also noteworthy that SIRT, SART, and CGLS result in several erroneously large Y-shifts around ~35°–40°, which show up as partial images with large regions of 0 signal when the individual XRM is inspected. It is unclear what causes this error; however, it is not expected to significantly impact the final reconstructed data as it only affected 2-3 XRMs. The evolution of the applied X and Y shifts as a function of iteration can be fully explored within the SI, with all reconstruction algorithms represented at 10, 20, 100, and 200 iterations in Supplementary Figures S8c,d, S9c,d respectively.

Next, we evaluate the sinogram post alignment and the 2D grayscale projection from the reconstructed 3D object (Figure 4) after 50 and 500 iterations. Sinograms (evaluated at a Y-value that corresponds to ~8 µm below the YSZ electrolyte) from each reconstruction algorithm are indicative of properly aligned data as the edges of features appear smooth and continuous, and no spiky or patchwork features indicative of improper alignment are present. The CGLS algorithm results in a slightly different appearance at high values of θ, as a distinct wave-like appearance is present at the edges of the high signal region (sample) from 90°–30° that is not observed with the other reconstruction algorithms. This suggests that using the CGLS reconstruction algorithm resulted in an alignment solution that had a subtle offset over tens of degrees, while images are well aligned with each other when only considering the nearest few neighboring XRMs. Additionally, there are discontinuities present at ~35°–40° which are most likely due to the error in Y-shifts observed in Figure 3. Overall, the convergence, applied shifts, and post-alignment sinograms suggest that each reconstruction algorithm successfully aligns the XRMs after 500 iterations despite the presence of some subtle differences

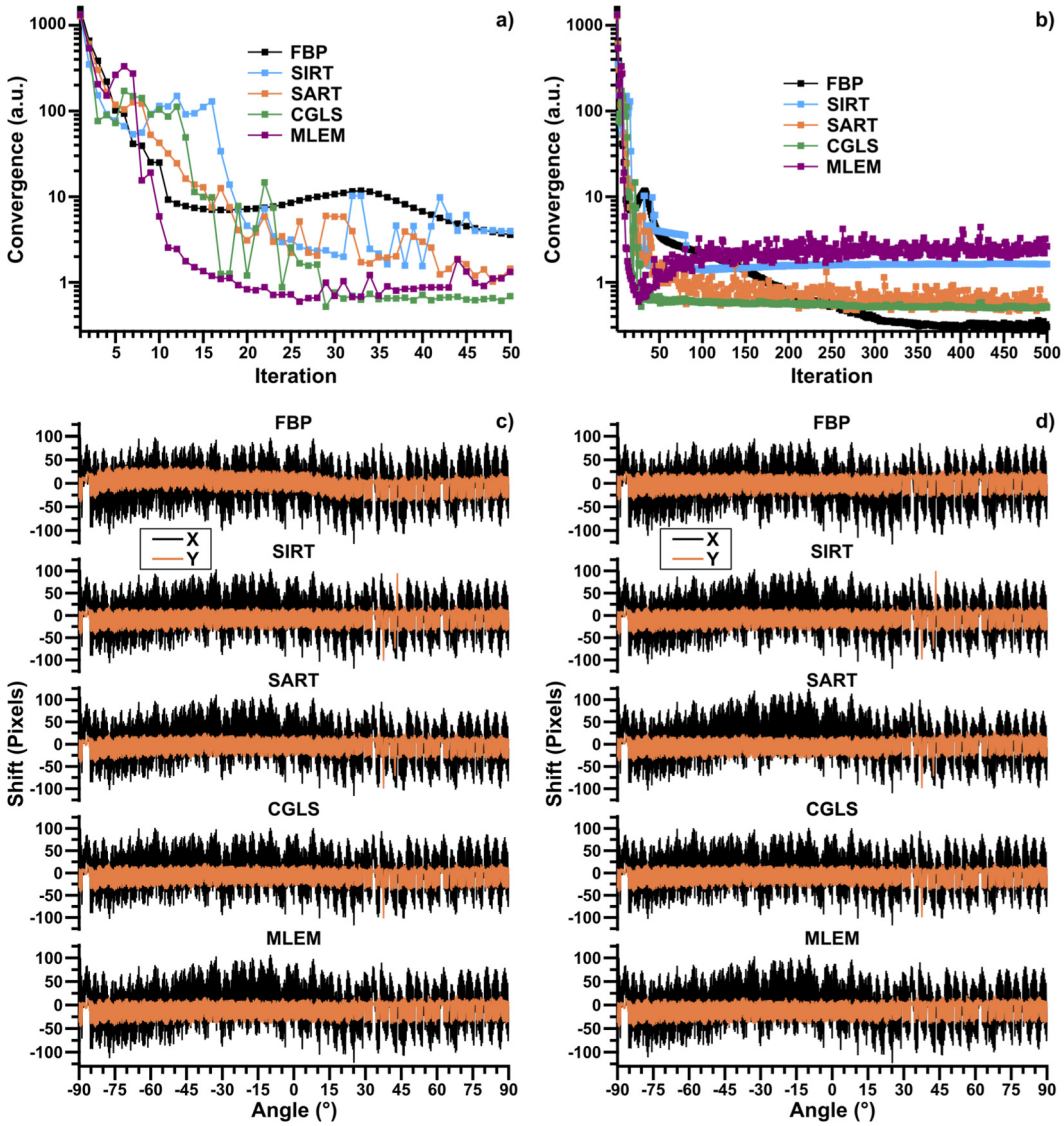

FIGURE 3
(a) Convergence (RMSE) plots after 50 iterations, and **(b)** following 500 iterations are shown alongside **(c)** the resulting X and Y shifts applied after 50 iterations, and **(d)** 500 iterations for all reconstruction algorithms.

and irregularities. Sinograms for each reconstruction algorithm at 10, 20, 100, and 200 iterations are available within the SI (Supplementary Figures S10a,c, S11a,c, respectively) and show the number of iterations that each reconstruction algorithm takes to no longer significantly change its alignment quality. The MLEM algorithm is the only one that yields a smooth, continuous sinogram after 10 alignment iterations (Supplementary Figure S10a), while all others show differing degrees of discontinuity (checkerboard or striped appearance) due to imperfectly aligned images. SIRT, SART, and CGLS reconstruction algorithms yield smooth sinograms after 20 iterations (Supplementary Figure S10c), although using CGLS results in the wave-like features that persist through to 500 alignment iterations. The alignment using FBP improves slightly from 10 to 20 iterations but still contains clear unaligned regions until 50 alignment iterations (Figure 4a) have been performed. Beyond 50 alignment iterations (Supplementary Figures S11a,c) minimal change in sinogram features occurs.

Grayscale projections were taken from the same slice and had the same contrast balancing applied to the image for each different reconstruction algorithm (Figures 4b,d) after 50 and 500 iterations. The FBP and CGLS algorithms can be grouped together as lower quality data while the SIRT, SART, and MLEM based alignments yielded much higher quality reconstructed data. This judgement is based on the clearly defined bright gray, dark gray, and black regions that are present within the SIRT, SART, and MLEM aligned data, with minimal speckling or streaking of different grayscales present within each feature. The FBP and CGLS aligned data have less well-defined boundaries between features and appear to have streaks present at the edges of the sample. By evaluating the grayscale projections for each reconstruction algorithm as a function of

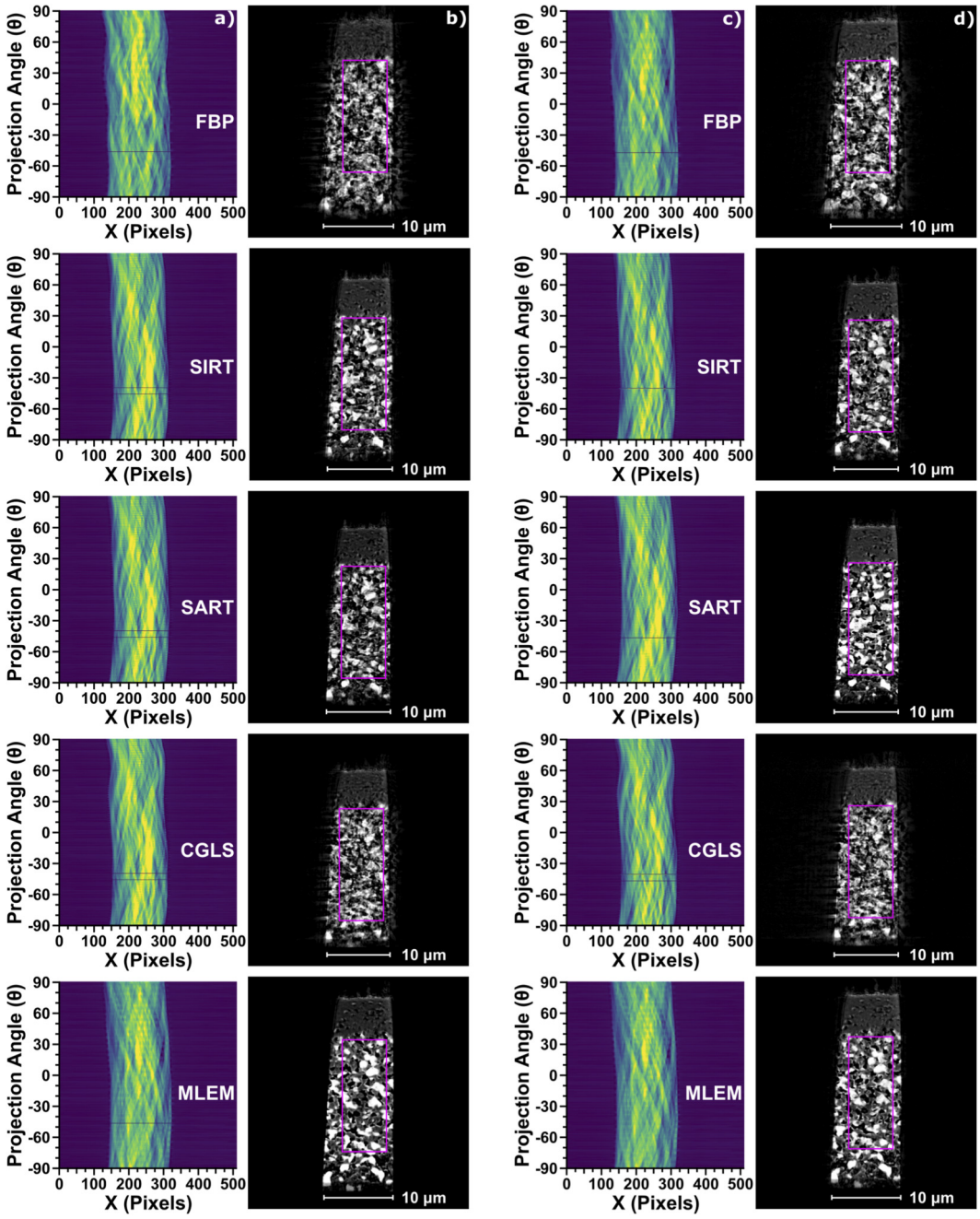

FIGURE 4
(a) Sinograms at a given Y-value ~8 μm below the Ni-YSZ/YSZ interface, and **(b)** 2D grayscale projections sliced parallel to the axial dimension near the center of the ROI are displayed for each reconstruction algorithm following 50 alignment iterations, and **(c,d)** again following 500 iterations. A pink rectangle is superimposed over the image to highlight the ROI from which grayscale histograms are constructed in Figure 5.

iteration, we see a clear difference in data quality improvement as a function of alignment iteration for the different reconstruction algorithms.

The MLEM algorithm aligned data shows clear feature definition after 10 alignment iterations (Supplementary Figure S10b) while all other algorithms do not result in clearly defined features in the 2D grayscale projections. After 20 iterations (Supplementary Figure S10d) and even more so after 50 iterations (Figure 4b), the material features become clearer and more well-defined for the SIRT and SART algorithm aligned data. However, the variance of grayscale intensity within each dataset's features remains much higher for the SIRT and SART algorithm aligned data than MLEM at equal alignment iterations. This progression of improving data quality continues through 100 iterations (Supplementary Figure S11b) and 200 iterations (Supplementary Figure S11d) for the SIRT and SART aligned datasets, while FBP and CGLS aligned data begins to appear to have discernible features in agreement with SIRT, SART, and

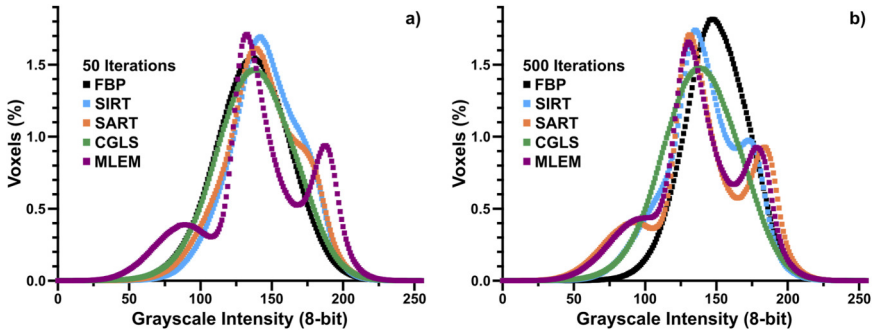

FIGURE 5
8-bit grayscale histograms extracted from reconstructed data following **(a)** 50 and **(b)** 500 iterations are displayed normalized to the total number of voxels in the cropped ROI highlighted in the respective 2D grayscale projection in Figure 4. ROIs are ~6 × 6 × 16 μm^3, consisting of ~26 million voxels.

MLEM aligned data after 200 iterations. However, feature clarity and intra-feature grayscale variation within FBP and CGLS aligned data does not improve to the same extent as SIRT, SART, or MLEM aligned data at any number of alignment iterations studied within.

While significant differences in feature/edge definition and the presence of artifacts/noise like speckling or streaking are clearly observable by eye in the grayscale projections, subtle differences in contrast and intra-region intensity variation are likely to be missed. Grayscale histograms can be used to quantitatively assess the variation in intensity that will be directly applicable to segmentation, and ultimately microstructure quantitative analysis accuracy and reliability. To produce the histograms displayed in Figure 5, the 3D reconstructed volume for a given alignment was cropped to an ~6 × 6 × 16 μm volume with the 16 μm dimension on the Y-axis and oriented such that no dense YSZ electrolyte is included in the cropped ROI, as highlighted in pink in Figure 4b. The intensity values were then converted from float to 8-bit and normalized to the total number of voxels in the ROI, typically ~26 million. After 50 alignment iterations (Figure 5a), using the MLEM reconstruction algorithm within this alignment framework yields a histogram with three well resolved peaks as each has a local minimum between itself and the next peak which will yield reliable 3-phase segmentation by histogram-based approaches. The SIRT and SART aligned data show a slight separation of a second peak to higher (brighter) grayscale values, and some asymmetry to lower values suggestive of the presence of three convolved peaks, however the lack of local minima separating the peaks makes this data clearly lower quality than the MLEM aligned data, in agreement with the 2D grayscale projections (Figure 4b). The histograms from FBP and CGLS aligned data are featureless, smooth curves and are not suitable for segmentation, clearly following the differences in feature clarity present in the 2D grayscale projections (Figure 4b).

After 500 alignment iterations (Figure 5b), the MLEM aligned data is no longer the highest quality as the local minimum between the dark and gray phases is at nearly the same voxel fraction as the peak maximum of the dark phase, resulting in many more uncertain voxels relative to isolating dark from gray phases. While it is challenging to definitively identify the difference by eye between the 2D grayscale projection for MLEM aligned data after 50 iterations (Figure 4b) and 500 iterations (Figure 4d), it is noteworthy that the RMSE for the MLEM algorithm continued to increase from ~25 iterations until it plateaued after 100 iterations, indicating a worsening of the convergence between reprojection and reconstructed data during alignment. The SART aligned data now has a histogram very similar to MLEM aligned data after 50 alignment iterations, with three well-resolved peaks separated by clear local minima. SIRT aligned data contains three peaks, but with only one local minimum, it is clearly lower quality than SART aligned data at 500 alignment iterations or MLEM aligned data at 50 alignment iterations. Even after 500 alignment iterations, using FBP and CGLS reconstruction algorithms within this alignment framework yields a relatively featureless histogram with no resolved contrast of grayscale values for reliable segmentation into the three phases present in these samples.

Histograms for each reconstruction algorithm used for 10, 20, 100, and 200 alignment iterations are present in Supplementary Figure S12. Histograms from MLEM aligned data show three clear peaks in as few as 10 alignment iterations, while all other reconstruction algorithms yield featureless histograms (Supplementary Figure S12a). After 20 alignment iterations the MLEM aligned data improves even more, as the local minima between each pair of peaks decreased, while all other reconstruction algorithms remain featureless (Supplementary Figure S12b). After 100 iterations, MLEM algorithm aligned data is very similar in quality, while the SIRT aligned data develops asymmetric features indicative of three grayscale peaks and SART aligned data has a clearly resolved bright-phase peak with a local minimum present between brightest and intermediate gray voxels (Supplementary Figure S12c). After 200 alignment iterations, the MLEM aligned data now yields a histogram with distinctly worse data quality, as the separation of intermediate gray and black peaks after 500 alignment iterations (Figure 5b) has become less clear. The decrease in y-axis separation between the peak maximum of the brightest peak and the local minimum between the brightest and intermediate peaks and the lack of local minimum between the intermediate and darkest peak provide evidence of the loss of data quality. This result agrees with the convergence plot (Figure 3b) which shows that the MLEM algorithm alignment increases in RMSE after reaching a minimum around 25 iterations and plateauing slightly after 100 alignment iterations. SIRT aligned data does not significantly change between 100 and 200 alignment iterations, while SART experiences a

very slight improvement as evidenced by the decrease in voxel fraction of the local minimum between its bright and intermediate intensity peaks (Supplementary Figure S12d). Alignments using FBP and CGLS algorithms do not yield histograms with sufficient quality to segment in any of the above results.

From the above analysis, using the MLEM reconstruction algorithm within this alignment framework yields the best data quality in the fewest iterations. This result is in agreement with the literature, in which MLEM outperformed GridREC (FBP based algorithm) and SIRT when applied to 3D phantoms with varying degrees of noise (Gürsoy et al., 2017). While SART is the fastest algorithm per iteration (Supplementary Figure S13), using the MLEM reconstruction algorithm yields excellent data quality in as little as 45 min (20 iterations), with optimal data quality taking 110 min (50 iterations). The next best performing reconstruction algorithm, SART, took 877 min (500 iterations) to match the data quality achieved using the MLEM algorithm in ~8× less time. To qualify computation time, workstation hardware is documented in Section 2.9. The only apparent disadvantage in using the MLEM reconstruction algorithm for XRM alignment is the increase in RMSE resulting in deteriorating data quality past 100 alignment iterations. While the difference in reconstruction algorithm performance with respect to data quality evaluated from 2D grayscale projections and histograms is clear, all algorithms performed relatively similar and appeared to successfully align the images when considering convergence, change in X and Y shifts, and sinogram features. This contradiction between alignment efficacy and data quality implies that either very subtle changes in alignment result in significant influence over grayscale image quality in the reconstructed volume, or that another factor influencing reconstructed data quality is evolving as a function of alignment iteration.

To investigate the first possibility, the difference in applied shifts is calculated versus the reconstruction algorithm that yielded the best data quality from histograms (Figure 5) for each algorithm after 50 alignment iterations (Supplementary Figure S14a) and 500 iterations (Supplementary Figure S14b). Comparing the difference of each reconstruction algorithm versus MLEM after 50 alignment iterations, each has a somewhat different difference profile in X-shifts, with FBP, SIRT, and SART displaying generally smooth profiles while CGLS has some jittery discontinuities at higher angles. On the Y-axis, FBP is offset by 10–20 pixels from −90 to 0 theta and shows variation at the tens of degrees scale, while SIRT, SART, and CGLS all have a relatively constant offset of ~5 pixels. SIRT, SART, and CGLS also have sharp peaks at a few angles between 35 and 45 theta which have been cut off on the Y-axis to preserve the scaling, as these aberrations were discussed previously. The discontinuities in X from CGLS and the varied offset in Y from FBP are indicative that these algorithms have not properly aligned the projections yet, whereas the smooth profiles for SIRT and SART with minor offsets suggest that these algorithms have properly aligned the data, with the offset relative to MLEM simply suggestive that each algorithm converges on a slightly different correct solution relative to where in X-Y space the projections are aligned to. After 500 alignment iterations, the SART aligned data is used as the baseline and Supplementary Figure S14b shows minimal discontinuities in the difference profile of X or Y shifts for any reconstruction algorithm. The only feature of note is the sinusoidal difference in CGLS applied X-shifts from −90 to −30 theta, which is also present after 50 iterations and was observed in the sinograms as well. From this analysis, we find it unlikely that constant offsets on the order of 5–10 pixels in Y, or gradual smooth offsets in X are likely to differentiate the alignment results enough to explain the significant difference in data quality as evaluated from grayscale histograms yielded by the different reconstruction algorithms after 50 and 500 alignment iterations.

3.3 Data quality dependence on algorithm

The differing levels of noise present in the reconstructed 3D datasets which reduce or completely conceal the contrast (peak separation) in Figure 5 can be more easily visualized by taking a 2D slice transverse to the axis of rotation and displaying it without any contrast adjustment (Figure 6). After 50 alignment iterations (Figure 6a), data aligned by FBP, SIRT, SART, and CGLS reconstruction algorithms all show differing amounts of noise in the grayscale projections, while the slice from 3D reconstructed data that was aligned using the MLEM reconstruction algorithm displays minimal noise and clearly defined dark gray, intermediate gray, and light gray features. This noise is most clearly seen at the edges of the sample where streaks are present, resulting in a spiky, many pointed star-shaped object when the known ground truth is a cylindrical smooth shape. Within the core of the sample these artifacts completely obscure any material features in the FBP and CGLS aligned data, while features are largely obscured in SIRT aligned data, and somewhat noisy but discernible in SART aligned data. After 500 alignment iterations (Figure 6b), both FBP and CGLS aligned data remain heavily impacted by star artifacts which obscure material features. SIRT aligned data improves significantly, but some noise is still present and the contrast is not as distinct as the data aligned with 50 MLEM iterations. SART appears to have no presence of star artifacts, and the features are clearly discernible throughout the transverse slice, in good agreement with Figure 5b. Interestingly, the data aligned using MLEM for 500 iterations appears to have had some subtle artifacts re-introduced, explaining the diminishing contrast in Figure 5b. This result highlights the importance of monitoring convergence when using MLEM and stopping the alignment before convergence increases excessively.

Calculating the SNR and CNR as shown in Figure 7 further supports the above findings. CGLS and FBP yield the lowest SNR (Figure 7a) after 50 iterations, while SIRT, SART, and MLEM algorithms result in progressively higher SNRs. The same trends are observed for CNR (Figure 7b). The trends remain largely the same after 500 iterations (Figures 7c,d), with one exception. After 500 iterations, CGLS now has the lowest SNR as FBP improved in quality from 50 to 500 iterations more than CGLS. As suggested above, MLEM does not improve from 50 to 500 iterations, with nearly the same SNR and CNR values presented. Additionally, after 500 iterations, SART has nearly identical CNR values as MLEM. This matches the results in Figures 5, 6. However, MLEM still yields slightly better SNR than SART for all phases after 500 iterations.

The performance of the five reconstruction algorithms can be attributed to their differing degrees of noise amplification/suppression during reconstruction and reprojection within the alignment framework. To highlight these differences, we first explore the analytical solution to tomographic reconstruction,

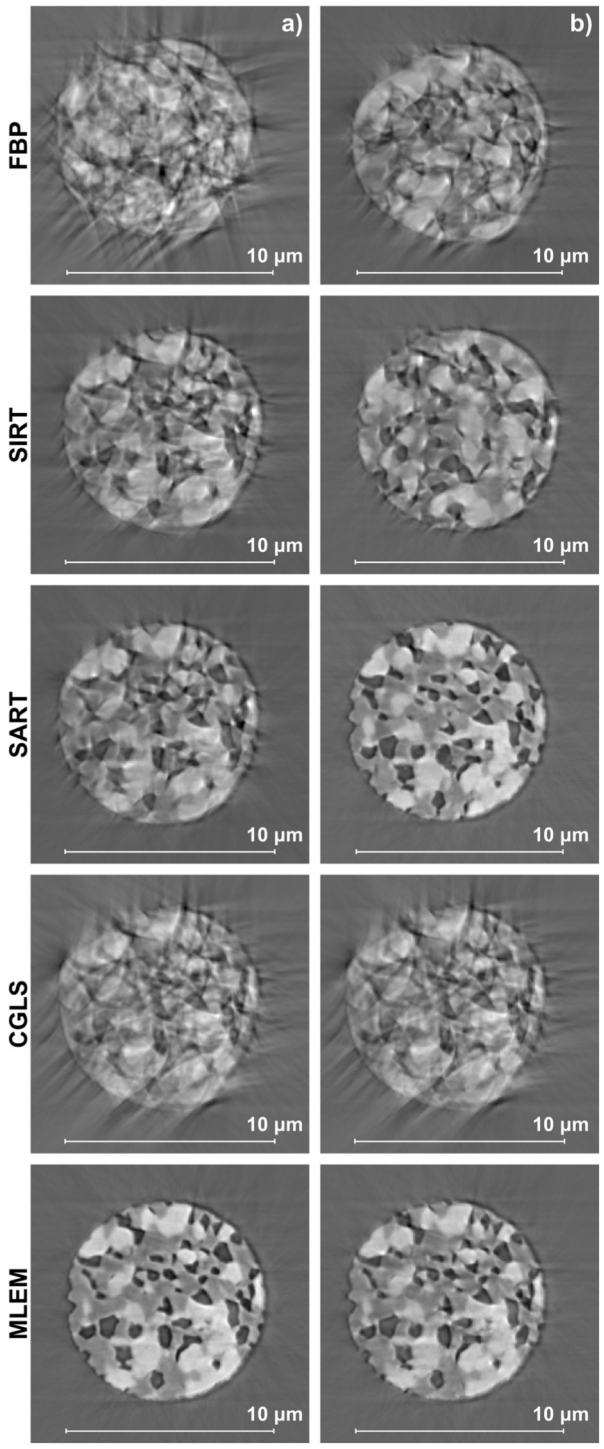

FIGURE 6
After **(a)** 50 alignment iterations and **(b)** 500 alignment iterations, 2D grayscale projections sliced in the transverse dimension are displayed with no contrast balancing.

which is visually depicted in the literature (Withers et al., 2021; Jacobsen, 2018). The analytical approach to tomographic reconstruction of many XRMs into a 3D object makes use of the Fourier Slice Theorem. A single XRM is essentially a 2D function containing the intensity value each detector pixel has measured, representing the 2D-array of X-ray attenuation coefficients of the material(s) the X-ray traveled through. Each row of intensity values can be projected into a 1D density distribution using the Radon transform at each distinct Y-value, which is done at all angles to produce a sinogram. These 1D projections are then transformed into Fourier space and assembled based on the angle the original XRM was collected at. Theoretically, an infinite number of angularly resolved projections would contain intersecting intensity information for all of frequency space, which can then be inverted using the inverse Fourier Transform to yield the 3D volume of the measured object. For a more detailed explanation and derivation, the reader is directed to the following literature (Algorithms for Reconstruction with Nondiffracting, 2001).

Two clear limitations are present within the analytical approach to tomographic inversion; an infinite number of projections cannot be taken, and when considering the intersection of all 1D projections in Fourier space, the intensity information overlaps disproportionately in the center. Perhaps the most historically ubiquitous reconstruction algorithm, FBP, attempts to remediate this overestimation issue (Algorithms for Reconstruction with Nondiffracting, 2001). A ramp filter was originally used to minimize this artifact, giving FBP its name. However in this work, FBP uses the Ram-Lak (Ramachandran and Lakshminarayanan, 1971) filter - numerous filters exist and over 15 are incorporated into TomoPyUI for an analyst to explore. The other main limitation of the analytical solution–the inability to take projections at infinite unique rotational angles–is further explored within the Crowther Criterion, which provides an answer to the query of how many angles is enough. The Crowther criterion (Crowther et al., 1970; Klug and Crowther, 1972) puts forth that an adequate number of projections such that intensity information completely covers all pixels when the intensity distribution is transformed from real space to transverse-axial Fourier space will enable accurate direct backprojection. This yields an equation which is presented in its simplest form in Equation 3, where N_θ is the number of projections, and N_{px} is the number of pixels on the detector's dimension parallel to the axis of rotation (in this case, the Y-axis).

$$N_\theta = \frac{\pi N_{px}}{2} \tag{3}$$

An excellent visual depiction of the Crowther criterion is present in reference (Jacobsen, 2018). For the detector settings used in this work (2048 pixels binning 2, so N_{px} = 1,024) a value of 1,608 is obtained for N_θ. Imaging was performed at 901 angles, and so the Crowther criterion was not satisfied in this work, which is often true in practice. This explains why the use of the FBP reconstruction algorithm within the joint iterative alignment framework does not yield high quality reconstructed data in this work. More detail on artifacts due to under sampling and other noise sources in CT is found in the literature (Aliasing Artifacts and Noise in, 2001).

In some cases, the Crowther criterion is ignored due to a lack of need for the highest practical resolution, when features of interest are much larger than the detector's pixel size. More applicable to this case, iterative reconstruction algorithms that transcend the limitations of reconstructions directly using the Radon transform have been developed which may not be impacted

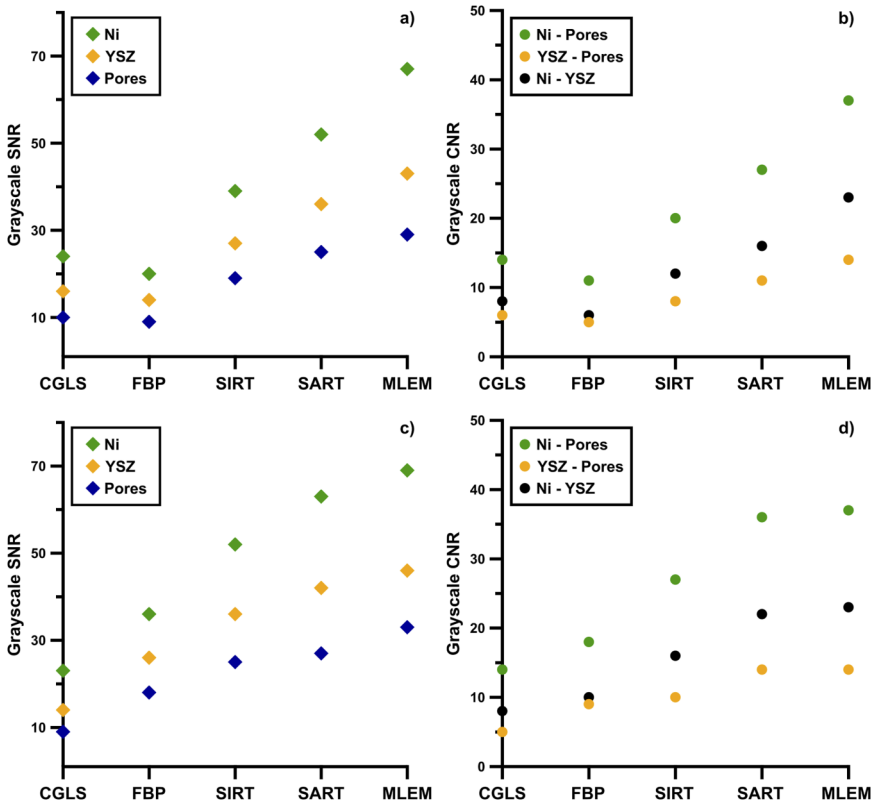

FIGURE 7
After **(a)** 50 alignment iterations the SNR is shown for each phase and reconstruction algorithm, along with **(b)** the corresponding CNR for each phase combination. After **(c)** 500 alignment iterations the SNR is shown for each phase and reconstruction algorithm, along with **(d)** the corresponding CNR for each phase combination. Reconstruction algorithms are ordered by increasing SNR after 500 iterations.

by a dataset having too few projections to satisfy the Crowther criterion–all of SIRT, SART, CGLS, and MLEM fall into this category. These algorithms take different approaches to solve the sparse data problem by producing a calculated dataset by interpolating the missing data and minimizing the difference between the measured and calculated data–SIRT and SART represent algebraic solutions while CGLS and MLEM are statistical solutions (Beister et al., 2012; Algebraic Reconstruction Algorithms, 2001; Gilbert, 1972). The SIRT algorithm uses information from all the projections simultaneously, differing from the earlier developed SART algorithm which uses information from only a single projection. Both of these algebraic techniques, along with the CGLS algorithm (May et al., 2021; Scales, 1987; Cools et al., 2015), can account for excessive noise through minimization of least squares and adjusting forward weighting factors while iterating. The MLEM algorithm (Dempster and Laird, 1977; Lange and Carson) uses a log-likelihood criterion to maximize reconstruction quality as the algorithm iterates, which is better equipped to deal with the stochastic nature of the data. It is likely that this significant difference in approach to minimizing the difference between measured and calculated data is responsible for how fewer iterations it takes the MLEM algorithm to produce a high-quality dataset than SART in this work. Historically, MLEM (and other iterative algorithms) have seen limited usage in tomography reconstruction due to excessively long compute times, however with the modern advances in parallel computation and the implementation of GPU based computations, using this statistical reconstruction algorithm within TomoPy's joint iterative reconstruction and reprojection alignment framework yields excellent data quality without onerously increasing the time per alignment iteration. While this approach presents an attractive outcome, the impact of interpolating methods (or future ML-based reconstruction/segmentation algorithms) on downstream property calculations like TPB density may be significant and when possible, collecting projections in excess of that recommended by the Crowther criterion remains advisable.

3.4 Reduced alignment time

Next, two additional parameters are explored to reduce total computation time needed to produce high contrast data. From the above analysis, the MLEM reconstruction algorithm is selected and used for 20 iterations. First, the amount of data used for the phase correlation step of the alignment is varied. In Section 3.2, the entirety of the dataset including >200 pixels of background on each side of the sample on the horizontal axis is used. An ~ 700 × 700 pixel ROI was selected such that the vertical edges of the sample and the horizontal interface between the Ni-YSZ and YSZ are included in the phase correlation subset as fiducials (ROI displayed in Supplementary Figure S15). The convergence and resulting histograms using the 700 × 700 pixel subset are

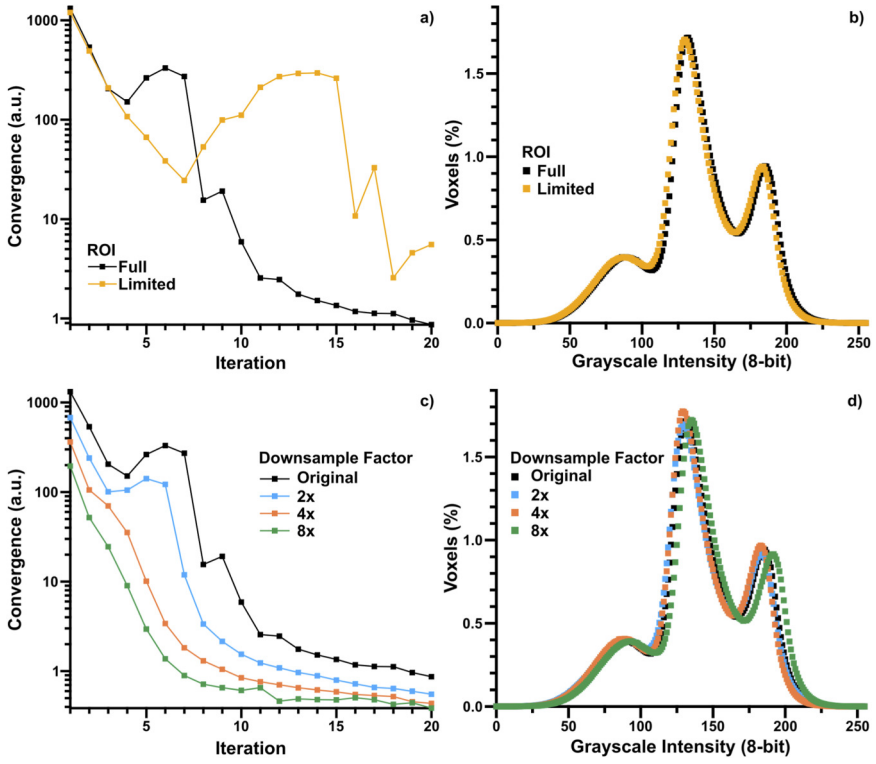

FIGURE 8
Alignment ROI impact on **(a)** convergence and **(b)** resulting grayscale histogram is displayed alongside the **(c)** convergence and **(d)** grayscale histogram of alignments performed using different downsample factors. In all cases, 20 alignment iterations using the MLEM reconstruction algorithm were performed.

compared to the full ROI in Figures 8a,b, respectively. Convergence appears to take more iterations with the smaller subset, as the RMSE reaches low values after a peak around 10–15 iterations. This slight difference in RMSE indicating slower convergence when using the smaller phase correlation ROI does not result in a loss of data quality, which is clearly displayed in Figure 8b. Very little difference in contrast is present within the histograms, with both showing clear separation of black, gray, and white peaks. The computation time for both alignments is essentially the same, at 45 min for the full ROI and 44 min for the smaller subset. Within the applied X and Y shifts (Supplementary Figure S16a) and final sinograms and 2D grayscale projections (Supplementary Figures S17a,b) no clear differences dependent on the subset size can be discerned. SNR and CNR values are displayed in Table 1. For all phases and phase combinations, the SNR and CNR values are slightly higher for the alignment using the full ROI. Additionally, an aggressively smaller subset (250 × 250 pixels) was also tried and did not successfully align the data in 20 iterations. Overall, there is minimal difference and no clear benefit gained from reducing the phase correlation subset size in this dataset despite the difference in convergence. Therefore, the full dataset ROI is used for the remaining alignments.

The second parameter varied to reduce computation time is the downsampling factor. In this case, pyramidal downsampling is performed with factors of 2× (512 × 512 pixels), 4× (256 × 256 pixels), and 8× (128 × 128 pixels), which are compared to the full resolution data (1,024 × 1,024 pixels). In Figure 8c, the convergence rate clearly decreases as resolution is decreased at higher downsampling factors. Following alignment, the data is returned to full resolution automatically, and the resulting grayscale histograms from the reconstructed volumes are compared in Figure 8d. There are some subtle differences, but overall, each histogram represents high contrast 3-phase data. At a downsample factor of 8×, the position of the black, gray, and white peaks is slightly shifted, and at a factor of 4×, the gray and white peak heights are slightly higher. No differences in applied X and Y shifts (Supplementary Figure S16b) or the final sinograms and 2D grayscale projections (Supplementary Figures S18a,b) are discernible for the different downsampling factors. Downsampling reduced the computation time from 2.25 min per iteration at the full resolution to 0.8, 0.4, and 0.25 min per iteration for each subsequently higher downsample factor. SNR and CNR values are presented in Table 1. Across the board, SNR values are very slightly lower for alignments performed using downsampling, although the 4× factor is nearly identical to the null case. In terms of CNR, the 4× downsample yields identical CNR as the null case, while 2× and 8× are very slightly lower than the null case. For this dataset, the loss of data quality up to an 8× downsample factor is minimal, and thus this setting is recommended, with the caveat that care must be taken not to use a downsampling factor that increases the downsampled pixel size beyond that of the feature sizes in the XRMs. As an example, the 8× downsampling factor increases the pixel size

TABLE 1 SNR and CNR values for Figure 8.

Alignment parameters	Ni SNR	YSZ SNR	Pores SNR	Ni-pores CNR	YSZ-pores CNR	Ni-YSZ CNR
Null (full ROI, original sampling)	69	46	30	39	16	23
Limited ROI	61	40	26	35	14	21
2× Downsample	63	42	28	36	14	22
4× Downsample	68	45	29	39	16	23
8× Downsample	64	42	28	36	14	22

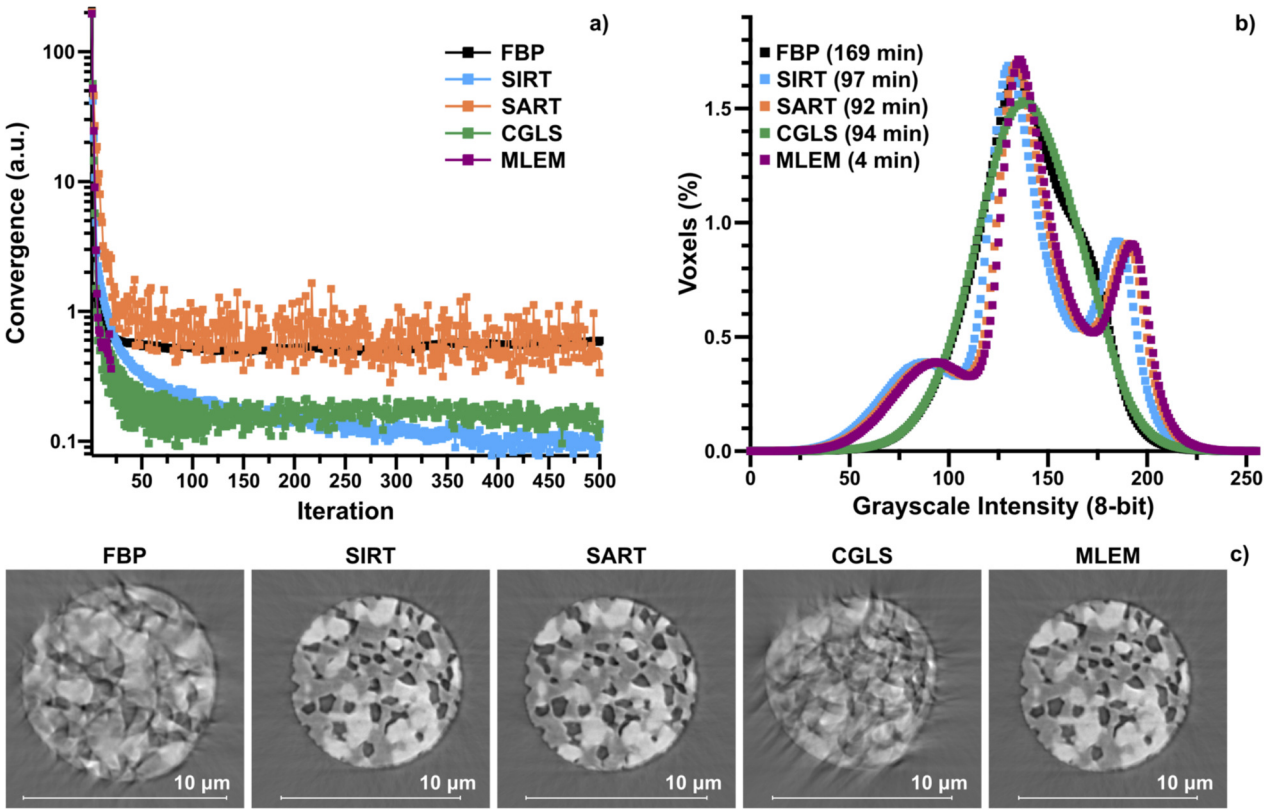

FIGURE 9
The results of each reconstruction algorithm used with its optimal settings are displayed, with **(a)** convergence, **(b)** grayscale histogram, and **(c)** 2D grayscale projections sliced in the transverse dimension with no contrast balancing presented.

in this work to ~229 nm, while the smallest average phase size is on the order of 350–400 nm, and so 8× is the largest factor used in this work to avoid obscuring most of the pore phase. Downsampling by 8× may average out some of the smallest regions, but adequate feature distinction remains to successfully align the XRMs and the data is returned to its original resolution after alignment. Any degree of downsampling drastically improves computation time and decreases the number of iterations needed to converge without negatively impacting the final data quality and should be explored for any dataset. However, if time is not a consideration and the most accurate, high SNR and CNR data is required, downsampling may need to be avoided. This is consistent with previous work on synthetic data and single phase samples using the same alignment framework (Gürsoy et al., 2017; Welborn et al., 2024).

3.5 Alignment with optimal settings

Combining the results of the above analyses, a final set of alignments were performed for each algorithm using its anticipated best settings. The full dataset ROI is used for alignment, and to accommodate more iterations, all algorithms were aligned with a downsampling factor of 8× applied. 500 iterations were used for each algorithm, excluding MLEM, which converges (Figure 9a) in much fewer iterations, and so MLEM was limited to 20 iterations to avoid increasing convergence as observed in Section 3.2. The resulting grayscale histograms are compared in Figure 9b. Each of SIRT, SART, and MLEM produce well defined, three-peak histograms, while FBP and CGLS still do not yield adequate contrast data. Transverse 2D slices of the grayscale 3D volume (Figure 9c) show

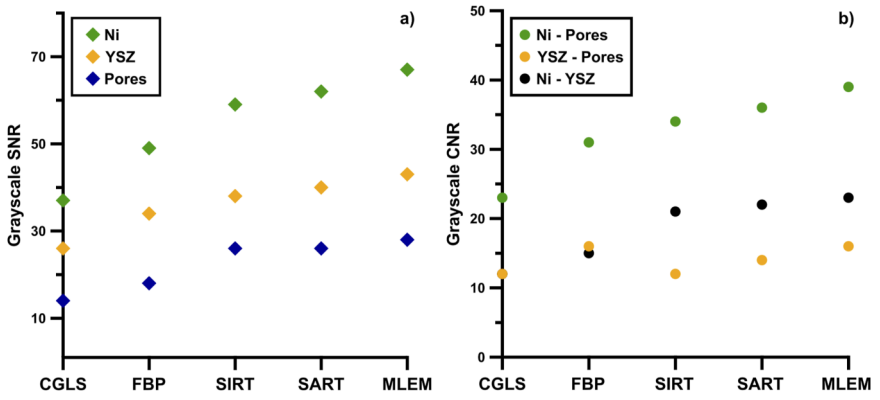

FIGURE 10
The SNR **(a)** is shown for each phase and reconstruction algorithm, along with **(b)** the corresponding CNR for each phase combination after alignment with optimal settings. Reconstruction algorithms are ordered by increasing SNR.

excellent resolution and contrast of features in the SIRT, SART, and MLEM data, while FBP and CGLS are still impacted by noise. Trends in SNR and CNR are presented in Figure 10. As in Figures 7c,d, CGLS yields the poorest data quality followed by FBP, SIRT, SART, and MLEM. While the histograms of SART and MLEM appear nearly identical, the SNR for MLEM is slightly better for each phase, and CNR is higher for MLEM, although the Ni–YSZ contrast is nearly identical.

The MLEM algorithm drastically outperforms the others in terms of speed due to the much lower number of iterations needed. The short computation time of 4 min to produce the highest quality data makes this iterative approach very accessible. This combination of settings is recommended as a starting point for alignment of similar datasets, while analyzing the convergence, applied X and Y shifts, sinogram, 2D grayscale projections, and histogram can be performed in a manner consistent with that displayed in Section 3.1 to optimize an alignment process specific to other materials, or Ni-YSZ with different feature attributes like particle size or different contrast due to varied X-ray energy or spatial resolution. There are, however, considerations for applying this result to significantly different datasets. Low contrast materials, such as different carbon structures are not easily distinguished in grayscale, and may result in different approaches or algorithms than those found optimal in this work. Synchrotron X-ray sources yield extremely high SNR data, and it is possible that lower SNR data from lab X-ray sources will have a different solution as the reconstruction algorithms may interact with lower SNR data differently if the number of projections taken are below that suggested by the Crowther criterion. The dramatic differences in data quality aligned using iterative reconstructions may not be present in lab X-ray source CT data. However, our workflow development approach and guidance towards evaluating CT data remains useful to a new analyst. Additionally, the development of ML-based tomographic reconstruction tools will likely change data processing approaches such as the one presented herein drastically. Effective adaptation of ML reconstruction, segmentation, and other processes will necessitate data quality inspection and rigorous oversight. This remains an area of need for more in-depth studies, particularly with lower SNR lab source CT data. Therefore, we view our results as a starting point for more rigorous studies with the intent to open data processing "black boxes" rather than simply replace them with more effective methods.

4 Conclusion

High contrast, low noise 3D reconstruction of a Ni-YSZ electrode from synchrotron nano-CT data collected at beamline 6-2c at SSRL is achieved with relatively low compute time by the workflow using TomoPyUI laid out in this article. A sensitivity analysis was performed on the projection alignment step, identifying that the reconstruction algorithm that converged the quickest while minimizing artifacts in the reconstructed data was MLEM, while the SART algorithm also yielded equal quality data, although many more alignment iterations were needed. Downsampling the data during alignment reduced the compute time by approximately an order of magnitude without detrimentally impacting the final data quality significantly, while also enabling the SIRT algorithm to produce data quality approaching that of the MLEM and SART algorithms. With three peaks present in the grayscale histogram and well-defined local minima between each, the uncertainty in assigning voxels to each phase through segmentation is adequately low for quantitative analysis. This method yields data clearly suitable for quantification of microstructural parameters including those with typically high variance such as TPB density.

While this particular workflow is likely to provide good results for similar datasets with high SNR and CNR, and sparse angular resolution below that recommended by the Crowther criterion, it should be expected that such a process may require continuous modification to adapt to differences in individual tomography datasets. Each piece of data may have different patterns and magnitude of shifts, different fluctuations in X-ray beam qualities, and different ground-truth features, all of which could impact the exact alignment settings needed to yield high quality data. Furthermore, data acquired at different X-ray energies or with significantly different signal values or referencing may require a different solution. Variations in feature size or distribution may also impact the alignment algorithms, and material sets with different

inherent contrast will significantly alter the features to be aligned. Therefore, this work is not meant to be a ubiquitous solution, rather to present a starting point for an analyst using nano-CT to solve a new problem, or for a new analyst to learn how to decide what parameters to vary in designing their own workflow, and how to evaluate their efficacy.

Data availability statement

The original contributions presented in the study are included in the article/Supplementary Material, further inquiries can be directed to the corresponding author.

Author contributions

MD: Conceptualization, Formal Analysis, Investigation, Writing – original draft, Writing – review and editing, Methodology, Visualization. SW: Writing – review and editing, Data curation, Software. CC: Writing – review and editing, Investigation, Methodology. MP: Investigation, Methodology, Writing – review and editing. HS: Methodology, Writing – review and editing. BG: Supervision, Writing – review and editing. JN: Methodology, Supervision, Writing – review and editing. SS: Conceptualization, Investigation, Methodology, Supervision, Writing – review and editing.

Funding

The author(s) declared that financial support was received for this work and/or its publication. Funding was provided by the U.S. Department of Energy's Office of Critical Materials and Energy Innovation (CMEI) Hydrogen and Fuel Cells Technology Office (HFTO) under the H2 from the Next-generation Electrolyzers of Water (H2NEW) consortium and the HydroGEN consortium. This work was authored in part by the National Laboratory of the Rockies for the U.S. Department of Energy (DOE) under Contract No. DE-AC36-08GO28308. The views expressed in the article do not necessarily represent the views of the DOE or the U.S. Government. The U.S. Government retains and the publisher, by accepting the article for publication, acknowledges that the U.S. Government retains a nonexclusive, paid-up, irrevocable, worldwide license to publish or reproduce the published form of this work, or allow others to do so, for U.S. Government purposes. Use of the Stanford Synchrotron Radiation Lightsource, SLAC National Accelerator Laboratory, is supported by the U.S. Department of Energy, Office of Science, Office of Basic Energy Sciences under Contract No. DE-AC02-76SF00515. This material is based on work supported by the US Department of Energy (DOE), Office of Science, Office of Workforce Development for Teachers and Scientists, Office of Science Graduate Student Research (SCGSR) program. The SCGSR program is administered by the Oak Ridge Institute for Science and Education (ORISE) for the DOE. ORISE is managed by ORAU (contract No. DE-SC0014664).

Conflict of interest

The author(s) declared that this work was conducted in the absence of any commercial or financial relationships that could be construed as a potential conflict of interest.

Generative AI statement

The author(s) declared that generative AI was not used in the creation of this manuscript.

Any alternative text (alt text) provided alongside figures in this article has been generated by Frontiers with the support of artificial intelligence and reasonable efforts have been made to ensure accuracy, including review by the authors wherever possible. If you identify any issues, please contact us.

Publisher's note

Supplementary material

The Supplementary Material for this article can be found online at: https://www.frontiersin.org/articles/10.3389/fenrg.2026.1801189/full#supplementary-material

References

Algebraic reconstruction algorithms (2001). In: *Principles of computerized tomographic imaging*. Society for Industrial and Applied Mathematics, 275–296. Available online at: https://epubs.siam.org/doi/abs/10.1137/1.9780898719277 (Accessed November 14, 2025).

Algorithms for reconstruction with nondiffracting sources (2001). *Principles of computerized tomographic imaging*. Society for Industrial and Applied Mathematic, 49–112. Available online at: https://epubs.siam.org/doi/abs/10.1137/1.9780898719277 (Accessed November 14, 2025).

Aliasing artifacts and noise in CT images (2001). In: *Principles of computerized tomographic imaging*. Society for Industrial and Applied Mathematics, 177–201. Available online at: https://epubs.siam.org/doi/abs/10.1137/1.9780898719277 (Accessed November 14, 2025).

Bailey, J. J., Heenan, T. M. M., Finegan, D. P., Lu, X., Daemi, S. R., Iacoviello, F., et al. (2017). Laser-preparation of geometrically optimised samples for X-ray nano-CT. *J. Microsc.* 267 (3), 384–396. doi:10.1111/jmi.12577

Beister, M., Kolditz, D., and Kalender, W. A. (2012). Iterative reconstruction methods in X-ray CT. *Phys. Med.* 28 (2), 94–108. doi:10.1016/j.ejmp.2012.01.003

Bertei, A., Ruiz-Trejo, E., Kareh, K., Yufit, V., Wang, X., Tariq, F., et al. (2017). The fractal nature of the three-phase boundary: a heuristic approach to the

degradation of nanostructured solid oxide fuel cell anodes. *Nano Energy* 38, 526–536. doi:10.1016/j.nanoen.2017.06.028

Chen, M., Liu, Y. L., Bentzen, J. J., Zhang, W., Sun, X., Hauch, A., et al. (2013). Microstructural degradation of Ni/YSZ electrodes in solid oxide electrolysis cells under high current. *J. Electrochem Soc.* 160 (8), F883–F891. doi:10.1149/2.098308jes

Chiu, W. K. S., De Angelis, S., Jørgensen, P. S., and Kuhn, L. T. (2024). Three-dimensional X-ray imaging and quantitative analysis of solid oxide cells. *Mater. Today* 80, 481–496. doi:10.1016/j.mattod.2024.08.016

Cocco, A. P., Nelson, G. J., Harris, W. M., Nakajo, A., Myles, T. D., Kiss, A. M., et al. (2013). Three-dimensional microstructural imaging methods for energy materials. *Phys. Chem. Chem. Phys.* 15 (39), 16377–16407. doi:10.1039/c3cp52356j

Cools, S., Ghysels, P., van Aarle, W., Sijbers, J., and Vanroose, W. (2015). A multi-level preconditioned Krylov method for the efficient solution of algebraic tomographic reconstruction problems. *J. Comput. Appl. Math.* 283, 1–16. doi:10.1016/j.cam.2014.12.044

Crowther, R. A., DeRosier, D. J., and Klug, A. (1970). The reconstruction of a three-dimensional structure from projections and its application to electron microscopy. *Proc. R. Soc. Lond Math. Phys. Sci.* 317 (1530), 319–340. doi:10.1098/rspa.1970.0119

Dempster, A. P., and Laird, N. M. (1977). Work(s): DBRR. Maximum likelihood from incomplete data *via* the EM algorithm. *J. R. Stat. Soc. Ser. B Methodol.* 39 (1), 1–38. doi:10.1111/j.2517-6161.1977.tb01600.x

Donath, T., Beckmann, F., and Schreyer, A. (206). *Image metrics for the automated alignment of microtomography data*. In: U. Bonse editor. San Diego, California, 631818. Available online at: http://proceedings.spiedigitallibrary.org/proceeding.aspx?doi=10.1117/12.679101 (Accessed January 15, 2025).

Gilbert, P. (1972). Iterative methods for the three-dimensional reconstruction of an object from projections. *J. Theor. Biol.* 36 (1), 105–117. doi:10.1016/0022-5193(72)90180-4

Gregor, J., and Benson, T. (2008). Computational analysis and improvement of SIRT. *IEEE Trans. Med. Imaging* 27 (7), 918–924. doi:10.1109/TMI.2008.923696

Guizar-Sicairos, M., Thurman, S. T., and Fienup, J. R. (2008). Efficient subpixel image registration algorithms. *Opt. Lett.* 33 (2), 156–158. doi:10.1364/OL.33.000156

Gürsoy, D., De Carlo, F., Xiao, X., and Jacobsen, C. (2014). TomoPy: a framework for the analysis of synchrotron tomographic data. *J. Synchrotron Radiat.* 21 (5), 1188–1193. doi:10.1107/S1600577514013939

Gürsoy, D., Hong, Y. P., He, K., Hujsak, K., Yoo, S., Chen, S., et al. (2017). Rapid alignment of nanotomography data using joint iterative reconstruction and reprojection. *Sci. Rep.* 7 (1), 11818. doi:10.1038/s41598-017-12141-9

Hauch, A., Küngas, R., Blennow, P., Hansen, A. B., Hansen, J. B., Mathiesen, B. V., et al. (2020). Recent advances in solid oxide cell technology for electrolysis. *Science* 370 (6513), eaba6118. doi:10.1126/science.aba6118

Heenan, T. M. M., Bailey, J. J., Lu, X., Robinson, J. B., Iacoviello, F., Finegan, D. P., et al. (2017). Three-phase segmentation of solid oxide fuel cell anode materials using lab based X-ray nano-computed tomography. *Fuel Cells* 17 (1), 75–82. doi:10.1002/fuce.201600176

Hsu, T., Epting, W. K., Mahbub, R., Nuhfer, N. T., Bhattacharya, S., Lei, Y., et al. (2018). Mesoscale characterization of local property distributions in heterogeneous electrodes. *J. Power Sources* 386, 1–9. doi:10.1016/j.jpowsour.2018.03.025

Iwai, H., Shikazono, N., Matsui, T., Teshima, H., Kishimoto, M., Kishida, R., et al. (2010). Quantification of SOFC anode microstructure based on dual beam FIB-SEM technique. *J. Power Sources* 195 (4), 955–961. doi:10.1016/j.jpowsour.2009.09.005

Jacobsen, C. (2018). Relaxation of the Crowther criterion in multislice tomography. *Opt. Lett.* 43 (19), 4811–4814. doi:10.1364/OL.43.004811

Joos, J., Carraro, T., Weber, A., and Ivers-Tiffée, E. (2011). Reconstruction of porous electrodes by FIB/SEM for detailed microstructure modeling. *J. Power Sources* 196 (17), 7302–7307. doi:10.1016/j.jpowsour.2010.10.006

Joos, J., Ender, M., Rotscholl, I., Menzler, N. H., and Ivers-Tiffée, E. (2014). Quantification of double-layer Ni/YSZ fuel cell anodes from focused ion beam tomography data. *J. Power Sources* 246, 819–830. doi:10.1016/j.jpowsour.2013.08.021

Jørgensen, P. S., Ebbehøj, S. L., and Hauch, A. (2015). Triple phase boundary specific pathway analysis for quantitative characterization of solid oxide cell electrode microstructure. *J. Power Sources* 279, 686–693. doi:10.1016/j.jpowsour.2015.01.054

Kak, A. C., and Slaney, M. (2001). "Reconstruction algorithms for parallel projections," in *Principles of computerized tomographic imaging* (Society for Industrial and Applied Mathematics). Available online at: http://epubs.siam.org/doi/book/10.1137/1.9780898719277 (Accessed September 8, 2025).

Kennouche, D., Chen-Wiegart, Y. chen K., Yakal-Kremski, K. J., Wang, J., Gibbs, J. W., Voorhees, P. W., et al. (2016a). Observing the microstructural evolution of ni-yttria-stabilized zirconia solid oxide fuel cell anodes. *Acta Mater.* 103, 204–210. doi:10.1016/j.actamat.2015.09.055

Kennouche, D., Chen-Wiegart, Y. chen K., Riscoe, C., Wang, J., and Barnett, S. A. (2016b). Combined electrochemical and X-ray tomography study of the high temperature evolution of Nickel – Yttria stabilized Zirconia solid oxide fuel cell anodes. *J. Power Sources* 307, 604–612. doi:10.1016/j.jpowsour.2015.12.126

Klug, A., and Crowther, R. A. (1972). Three-dimensional image reconstruction from the viewpoint of information theory. *Nature* 238, 435–440.

Laguna-Bercero, M. A. (2012). Recent advances in high temperature electrolysis using solid oxide fuel cells: a review. *J. Power Sources* 203, 4–16. doi:10.1016/j.jpowsour.2011.12.019

Lange, K., and Carson, R. *EM reconstruction algorithms for emission and transmission tomography*. New York: Raven Press.

Liu, Y., Meirer, F., Williams, P. A., Wang, J., Andrews, J. C., and Pianetta, P. (2012). *TXM-Wizard*: a program for advanced data collection and evaluation in full-field transmission X-ray microscopy. *J. Synchrotron Radiat.* 19 (2), 281–287. doi:10.1107/S0909049511049144

Lu, X., Heenan, T. M. M., Bailey, J. J., Li, T., Li, K., Brett, D. J. L., et al. (2017). Correlation between triple phase boundary and the microstructure of solid oxide fuel cell anodes: the role of composition, porosity and Ni densification. *J. Power Sources* 365, 210–219. doi:10.1016/j.jpowsour.2017.08.095

Mahbub, R., Hsu, T., Epting, W. K., Nolan, G., Lei, Y., Nuhfer, N. T., et al. (2021). Quantifying morphological variability and operating evolution in SOFC anode microstructures. *J. Power Sources* 498, 229846. doi:10.1016/j.jpowsour.2021.229846

May, K. H., Keil, A., Von Freymann, G., and Friederich, F. (2021). The conjugate gradient least square algorithm in terahertz tomography. *IEEE Access* 9, 142168–142178. doi:10.1109/ACCESS.2021.3116801

Mogensen, M. B., Hauch, A., Sun, X., Chen, M., Tao, Y., Ebbesen, S. D., et al. (2017). Relation between Ni particle shape change and Ni migration in Ni–YSZ electrodes – a hypothesis. *Fuel Cells* 17 (4), 434–441. doi:10.1002/fuce.201600222

Mogensen, M. B., Chen, M., Frandsen, H. L., Graves, C., Hauch, A., Jacobsen, T., et al. (2019). Comprehensive hypotheses for degradation mechanisms in Ni-Stabilized zirconia electrodes. *ECS Trans.* 91 (1), 613–620. doi:10.1149/09101.0613ecst

Mogensen, M. B., Chen, M., Frandsen, H. L., Hauch, A., Hendriksen, P. V., Jacobsen, T., et al. (2020). *Review of Ni migration in SOC electrodes*. New York: Raven Press.

Mogensen, M. B., Chen, M., Frandsen, H. L., Graves, C., Hauch, A., Hendriksen, P. V., et al. (2021). Ni migration in solid oxide cell electrodes: review and revised hypothesis. *Fuel Cells* 21 (5), 415–429. doi:10.1002/fuce.202100072

Nelson, G. J., Grew, K. N., Izzo, J. R., Lombardo, J. J., Harris, W. M., Faes, A., et al. (2012). Three-dimensional microstructural changes in the Ni–YSZ solid oxide fuel cell anode during operation. *Acta Mater.* 60 (8), 3491–3500. doi:10.1016/j.actamat.2012.02.041

Pelt, D. M., Gürsoy, D., Palenstijn, W. J., Sijbers, J., De Carlo, F., and Batenburg, K. J. (2016). Integration of TomoPy and the ASTRA toolbox for advanced processing and reconstruction of tomographic synchrotron data. *J. Synchrotron Radiat.* 23 (3), 842–849. doi:10.1107/S1600577516005658

Ramachandran, G. N., and Lakshminarayanan, A. V. (1971). Three-dimensional reconstruction from radiographs and electron micrographs: application of convolutions instead of fourier transforms. *Proc. Natl. Acad. Sci. U. S. A.* 68 (9), 2236–2240. doi:10.1073/pnas.68.9.2236

Rocklin, M.(2915). Dask: parallel computation with blocked algorithms and task scheduling. Austin, Texas, 126–132. Available online at: https://doi.curvenote.com/10.25080/Majora-7b98e3ed-013 (Accessed March 19, 2026).

Scales, J. A. (1987). Tomographic inversion *via* the conjugate gradient method. *GEOPHYSICS* 52 (2), 179–185. doi:10.1190/1.1442293

Shearing, P. R., Bradley, R. S., Gelb, J., Tariq, F., Withers, P. J., and Brandon, N. P. (2012). Exploring microstructural changes associated with oxidation in Ni–YSZ SOFC electrodes using high resolution X-ray computed tomography. *Solid State Ion.* 216, 69–72. doi:10.1016/j.ssi.2011.10.015

Shepp, L. A., Hilal, S. K., and Schulz, R. A. (1979). The tuning fork artifact in computerized tomography. *Comput. Graph Image Process* 10 (3), 246–255. doi:10.1016/0146-664X(79)90004-2

Shri Prakash, B., Senthil Kumar, S., and Aruna, S. T. (2014). Properties and development of Ni/YSZ as an anode material in solid oxide fuel cell: a review. *Renew. Sustain Energy Rev.* 36, 149–179. doi:10.1016/j.rser.2014.04.043

Slomski, H. S., Kaufman, J. L., Dzara, M. J., Strange, N. A., Priest, C., Hartvigsen, J. L., et al. (2025). Understanding $(La,Sr)(Co,Fe)O_{3-\delta}$ phase instability within SOECs using a combined experimental and atomistic modeling approach. *ACS Phys. Chem. Au* 10, 4c00095-218. doi:10.1021/acsphyschemau.4c00095

Stankevič, T., Engblom, C., Langlois, F., Alves, F., Lestrade, A., Jobert, N., et al. (2017). Interferometric characterization of rotation stages for X-ray nanotomography. *Rev. Sci. Instrum.* 88 (5), 053703. doi:10.1063/1.4983405

Tan, K. S., Lam, C. K., Tan, W. C., Ooi, H. S., and Lim, Z. H. (2024). A review of image processing and quantification analysis for solid oxide fuel cell. *Energy AI.* 16, 100354. doi:10.1016/j.egyai.2024.100354

Trini, M., Jørgensen, P. S., Hauch, A., Bentzen, J. J., Hendriksen, P. V., and Chen, M. (2019). 3D microstructural characterization of Ni/YSZ electrodes exposed to 1 year of electrolysis testing. *J. Electrochem Soc.* 166 (2), F158–F167. doi:10.1149/2.1281902jes

Trini, M., Hauch, A., De Angelis, S., Tong, X., Hendriksen, P. V., and Chen, M. (2020). Comparison of microstructural evolution of fuel electrodes in solid oxide fuel cells and electrolysis cells. *J. Power Sources* 450, 227599. doi:10.1016/j.jpowsour.2019.227599

van Aarle, W., Palenstijn, W. J., Cant, J., Janssens, E., Bleichrodt, F., Dabravolski, A., et al. (2016). Fast and flexible X-ray tomography using the ASTRA toolbox. *Opt. Express* 24 (22), 25129–25147. doi:10.1364/OE.24.025129

Wang, C. C. (2020). Joint iterative fast projection matching for fully automatic marker-free alignment of nano-tomography reconstructions. *Sci. Rep.* 10 (1), 7330. doi:10.1038/s41598-020-62949-1

Wang, J., chen, K. C. Y., Yuan, Q., Tkachuk, A., Erdonmez, C., Hornberger, B., et al. (2012). Automated markerless full field hard x-ray microscopic tomography at sub-50 nm 3-dimension spatial resolution. *Appl. Phys. Lett.* 100 (14), 143107. doi:10.1063/1.3701579

Wang, Y., Li, W., Ma, L., Li, W., and Liu, X. (2020). Degradation of solid oxide electrolysis cells: phenomena, mechanisms, and emerging mitigation strategies—A review. *J. Mater. Sci. Technol.* 55, 35–55. doi:10.1016/j.jmst.2019.07.026

Welborn, S. S., Preefer, M. B., and Nelson Weker, J. (2024). *TomoPyUI*: a user-friendly tool for rapid tomography alignment and reconstruction. *J. Synchrotron Radiat.* 31 (4), 979–986. doi:10.1107/S1600577524003989

Withers, P. J., Bouman, C., Carmignato, S., Cnudde, V., Grimaldi, D., Hagen, C. K., et al. (2021). X-ray computed tomography. *Nat. Rev. Methods Primer* 1 (1), 18. doi:10.1038/s43586-021-00015-4

Wolf, S. E., Winterhalder, F. E., Vibhu, V., de Haart, L. G. J., Guillon, O., Eichel, R. A., et al. (2023). Solid oxide electrolysis cells – current material development and industrial application. *J. Mater. Chem. A* 11 (34), 17977–18028. doi:10.1039/D3TA02161K

Zhu, Z., Slomski, H. S., Dzara, M. J., Crain, C. A., Strange, N. A., Ginley, D. S., et al. (2025). Voltage cycling as a dynamic operation mode for high temperature electrolysis solid oxide cells. *J. Power Sources* 642, 236958. doi:10.1016/j.jpowsour.2025.236958

Zhu, Z., Dzara, M. J., Slomski, H., Van Winkle, M., Hathaway, O., Nagle-Cocco, L. A. V., et al. (2026). Robust dynamic operation of high temperature electrolysis solid oxide cells. *J. Power Sources* 674, 239770. doi:10.1016/j.jpowsour.2026.239770